Evolving magma temperature and volatile contents over the 2008-2018 summit eruption of Kīlauea Volcano

Josh Crozier,[1,2*] Leif Karlstrom,[1]

[1]Department of Earth Sciences, University of Oregon,
Eugene, OR, USA.
[2]now at U.S. Geological Survey California Volcano Observatory
Moffett Field, CA, USA.

*Corresponding author. E-mail: jcrozier@usgs.gov

Magma rheology and volatile contents exert primary and highly nonlinear controls on volcanic activity. Subtle changes in these magma properties can modulate eruption style and hazards, making in situ inference of their temporal evolution vital for volcano monitoring. Here we study thousands of impulsive magma oscillations within the shallow conduit and lava lake of Kīlauea Volcano, Hawai'i, USA over the 2008-2018 summit eruptive sequence, encoded by 'Very-Long-Period' seismic events and ground deformation. Inversion of these data with a petrologically informed model of magma dynamics reveals significant variation in temperature and highly disequilibrium volatile contents over days to years, within a transport network that evolved over the eruption. Our results suggest a framework for inferring subsurface magma dynamics associated with prolonged eruptions in near real time that synthesizes petrologic and geophysical volcano monitoring approaches.

One-Sentence Summary

Resonant magma oscillations reveal evolving magma properties over a decade long eruption at Kīlauea Volcano, Hawai'i, USA.

Introduction

Kīlauea volcano, Hawai‘i, USA, is one of the most active, best monitored, and best studied volcanoes on Earth (*1*), serving as a focal point for volcanologic research (*2*). However, resolving in situ variation in subsurface magma dynamics remains a challenge at Kīlauea and volcanoes globally (*3*). The 2008-2018 Kīlauea summit eruption represents an opportunity to address this knowledge gap. The eruption involved a persistent lava lake in the Halema‘uma‘u summit vent and multiple subsurface magma intrusions and East Rift Zone eruptions, ending with a spectacular caldera collapse sequence representing the highest historical sustained eruption rate at Kīlauea (*4–6*). Previous studies suggested the main Kīlauea shallow summit magma plumbing system during this time consisted of the 1-2 km deep Halema‘uma‘u reservoir and the 3-5 km deep South Caldera reservoir (Fig. 1) (*7, 8*). The Halema‘uma‘u reservoir and overlying lava lake were continuously connected (*4*) by a $\sim$10 m wide conduit (*9*). Magma passed through the summit en route to the East Rift Zone, although the nature of hydraulic connections between the summit reservoirs, rift zone, and deeper magma sources are not well known (*8, 10*).

A wide range of data, interpreted using physical and chemical models, inform this picture of magma dynamics. Transport geometry is constrained primarily through inversion of seismic and geodetic data (*7, 9, 11*). Continuous gravity data are only available over limited time segments, but constrain the density of magma in the lava lake and suggest temporal variation of up to 1500 kg/m^3 (*12*). Analysis of erupted products provides limited temporal and spatial resolution, but suggests Halema‘uma‘u magma consists of near-liquidus (1150-1300 °C) crystal-poor basalt outgassed in CO_2 with respect to the primary mantle magma (*13, 14*). Subsurface magma volatile contents are also indirectly informed by continuous gas emissions (*13, 15, 16*). These analyses suggest significant disequilibrium outgassing, or mechanical decoupling of gas bubbles from melt due to continuous convecting and outgassing (*17*). However, geochemical and geophysical data are rarely combined in a quantitative manner.

Very-Long-Period (VLP) seismicity, with energy concentrated at periods above 2 s, has the potential to help unify these diverse constraints. VLP seismicity is prevalent at many volcanoes and often inferred to represent transient magma flow (*18*), thus directly probing magma properties and transport geometry in ways not readily obtainable by other geophysical analyses. VLP signals are part of a spectrum of oscillatory motions that can result from impulsive or continuous forcing of magma transport structures (*19, 20*), but the VLP band is advantageous due to being less sensitive to path distortions from heterogeneous earth structure than shorter period signals.

Multiple resonant modes have been identified at Kīlauea, but the dominant VLP signal is from ‘conduit-reservoir’ resonance in which stratified magma in the conduit and lake sloshes in and out of the underlying reservoir (*9, 21, 22*) (Fig. 1). This resonance occurs sometimes as continuous tremor but most often as discrete minutes-long events triggered both from the lake surface (such as via rockfalls from the crater walls) and from depth (*22, 23*). Oscillation restoring forces are from gravity and magma reservoir elasticity, while damping is from viscous drag on the conduit walls. Resonant period is primarily sensitive to conduit length and bulk magma density/density stratification (*9*). Decay rate is quantified by quality factor (the ratio of energy stored per cycle over energy lost per cycle) and is primarily sensitive to conduit radius and apparent magma viscosity. In the shallow Halemaʻumaʻu magma system, where melt composition doesn't vary much in time or space and where crystal contents are low (*13, 14, 24*), magma density is primarily controlled by porosity and magma viscosity is primarily controlled by porosity and temperature. In chemical equilibrium, gas mass fraction (hence porosity) depends upon total volatile mass fraction and pressure-dependent solubility of dominant volatile species (H_2O, CO_2, and sulfur) (*25*).

VLP seismicity at Kīlauea thus reflects evolving magma thermal and chemical state as well as transport structures. Over the 2008-2018 Kīlauea eruption, thousands of conduit-reservoir resonance events provide an unprecedented record of time-evolving subsurface magma transport.

Approach: Inferring magma properties from geophysical data

Fig. 2 outlines our workflow. We first conduct kinematic elastic inversions between 2008-2018 of continuous Global Navigation Satellite System (GNSS) ground deformation data (*26*) (Fig. S3, S4) for shallow magma reservoir pressure histories. In particular, Halemaʻumaʻu reservoir pressure constrains magma column density in the overlying summit lava lake and conduit. Summit deformation at Kīlauea is complex: to resolve Halemaʻumaʻu reservoir pressure we build on constraints from previous geodetic studies (*7, 11, 27*) and include three known deformation sources (*26*).

We next use a perturbation approach to model transient flow associated with conduit-reservoir magma resonance (*26*) (Fig. 1), extending previous analyses (*9, 21*). We treat fluid properties of the multi-phase magma as functions of magmastatic pressure (an approximation given slow exchange flow within the conduit/lava lake (*28*)), temperature, and vertically stratified total volatile mass fractions (CO_2+H_2O, Fig. 1, S2), neglecting crystals and assuming an average melt composition based on 2008-2010 Halemaʻumaʻu samples (*13, 25, 29–31*). We use this model to invert for magma properties from Halemaʻumaʻu reservoir pressure, lava lake elevation and areal extent (*4, 32*), and the resonant period and quality factor of VLP seismic events cataloged over 2008-2018 by (*22*) (Fig. 2) (*26*).

Resolving time evolution of shallow magma properties at Kīlauea is a long-standing challenge (*9, 33, 34*). We focus on shorter term changes in multiphase magma properties by assuming a fixed magma system geometry based on previous inversions (*7, 9, 11*). Four additional assumptions are made to facilitate unique inversions for magma properties (*26*) (supplementary text): 1. Temperature is spatially uniform in the conduit and lake. This is justified because the conduit undergoes quasi-steady exchange flow/mixing (*35*) and the lake contributes negligibly to viscous damping. 2. Magma in the conduit/lake has a fixed total (dissolved+exsolved) H_2O/CO_2 mass ratio. Volatile composition could vary over time, but is unconstrained in our model without additional data so we fix volatile ratios based on erupted products and gas emissions (*13, 14, 36*). 3. Total volatile mass fraction varies linearly with depth (Fig. 1) subject to stable stratification which should be approximately valid for the largely quiescent magma column. 4. Total volatile mass fraction at the lake surface is constant. While there is known to be some variation in porosity near the lake surface from continuous gravity data (*37*), these data are not available over most of the timespan. Additionally, our model exhibits minimal sensitivity to density stratification within the lake; it is primarily sensitive to average density (which controls the magmastatic pressure load of the lake on the conduit).

We test different fixed parameter combinations and conduct an a posteriori assessment of these assumptions. The magma properties we invert for are: 1. magma temperature, 2. conduit average total volatile mass fraction X^{avg}, and 3. total volatile mass fraction stratification (difference between conduit top and conduit bottom) ΔX. We note that while the magma temperature parameter is applied to the whole magma column, the model is primarily sensitive to conduit temperature. We also note that due to tradeoffs between volatile contents at the bottom and top of the lava lake, ΔX should be considered to represent a general volatile stratification over the whole magma column (conduit and lava lake).

Results

For our reference fixed parameters, Fig. 3 shows the timeline of GNSS inversion results and VLP magma resonance inversion results, along with other data. Shaded regions in Fig. 3 show the envelope of inversion results obtained by varying individual fixed parameters over feasible ranges, as detailed in the supplementary text (Fig. S5). Evolution of magma system geometry, which is not considered in our inversions, is more likely to affect trends in inversion results over long (year or more) timescales. In particular, inversion results with the reference fixed parameters are likely not reliable in 2009-early 2010 and mid 2011 (discussion). On short timescales, noise in input data likely contributes to scatter and outliers in the inversion results. We thus focus most analysis on temporally averaged values, and in particular on the relative variability in these values over timescales of a year or less rather than their absolute value at a given time. Fig. 4 shows amplitude spectra, coherence, and phase lags between data sets with 95% significance thresholds (supplementary text). Additional analyses are shown in Fig. S6, S7, and S8.

As expected for an open-vent magma system, Halema‘uma‘u reservoir pressure is well correlated with lava lake elevation over timescales from days to about a year (Fig. 3, 4) (*4, 22*). Strong coherence between Halema‘uma‘u and South Caldera reservoir pressures over timescales of days to months (Fig. 4, S6) suggests that magma is often transferred between the reservoirs, although the anticorrelation implies hydraulic disequilibrium. This could indicate an intermittent connection, consistent with the unsteady connectivity inferred during hours-days long “deflation-inflation” events (*6, 8, 38*). We are not aware of any other settings where a consistent anticorrelation is observed between different magma reservoirs at the same volcano, although intermittent hydraulic connections have been inferred between Kīlauea and Mauna Loa (*39*), as well as at other volcanoes such as Soufriére Hills (*40*) and Etna (*41*).

Different fixed parameters affect the absolute value of inverted magma temperature, but the pattern of relative temporal variation is robust and the magnitude of such changes varies by less than ∼20 °C (Fig. 3, S5). Inverted temperature is primarily sensitive to conduit radius; decreasing radius by 10 m (to 5 m) uniformly increases temperatures by ∼60 °C while increasing radius by 10 m (to 25 m) uniformly decreases temperatures by ∼40 °C. Conduit magma temperatures span the full 1150-1300 °C range of Halema'uma'u magma storage temperatures previously estimated from ejecta geothermometry (*13,24*), although it is difficult to make a direct comparison given uncertainty in the depths and/or timescales recorded by geothermometers.

On timescales from days-months, temperature exhibits up to 100 °C variation (Fig. 3), corresponding to up to an order of magnitude variation in magma viscosity (Fig. S2, S8). Temperature and resonant quality factor are strongly correlated (Fig. S6), which suggests that temperature is a primary driver of variations in magma viscosity. The dominance of temperature is unexpected because porosity has previously been proposed as a likely source of variation in VLP quality factor (*21*) and is known to vary significantly as bubbles rise and accumulate (*28, 37*).

Different fixed parameters affect the inverted absolute value of X^{avg} by up to $\sim$1 wt%, but the pattern of relative temporal variation is robust and the magnitude of such changes varies by less than $\sim$0.4 wt% (Fig. 3, S5). Similarly, different fixed parameters affect the inverted absolute value of ΔX by up to $\sim$1 wt%, but the pattern of relative temporal variation is robust and the magnitude of such changes varies by less than $\sim$0.2 wt% (Fig. 3, S5). Over most of the timeline X^{avg} is greater than the inferred primary magma volatile mass fraction of 1-2 wt%, a notable accumulation particularly since some of the primary CO_2 may have already been lost at depth (*14, 36, 42*). Additionally, ΔX is mostly similar to or larger than inferred primary magma volatile mass fraction. Together these indicate significant departures from equilibrium outgassing, with an accumulation of volatiles in the upper conduit and lava lake.

On timescales of days-months, X^{avg} varies by up to $\sim$0.6 wt% and ΔX varies by up to $\sim$1 wt% (Fig. 3). That this temporal variation is similar to the inferred primary magma's total volatile mass fraction of 1-2 wt% (*36, 42*) suggests significant variations in the outgassing regime (*14*). The only volatile species with continuous emission measurements that can be compared with ΔX and X^{avg} is SO_2. SO_2 has roughly similar solubility to H_2O in mafic melts (*43*) and so will approximately trade-off with H_2O in our model. SO_2 emissions exhibit strong variation (an order of magnitude or more) on timescales from days to years (*15, 16*). We do not observe consistently strong coherence between ΔX or X^{avg} and SO_2 emissions (Fig. S6), although several pronounced increases in either ΔX or X^{avg} do correspond to increases in SO_2 (e.g., Apr 2015, Jan 2016, Oct 2016, and Aug 2017). Inconsistent coherence could partly reflect the high uncertainty in SO_2 emission data, although we note that gas emissions from the lava lake surface will not necessarily directly correlate with the amount of volatiles accumulated in the magma column. In fact, the strong in-phase coherence between Halema'uma'u reservoir pressure (or lava lake elevation) and ΔX on timescales of less than 90 days (Fig. 4) suggests that volatiles build up in the upper conduit/lake as magma accumulates in the Halema'uma'u system, rather than maintaining a steady volatile mass balance through the shallow magma column. This could reflect an increase in volatile flux (e.g., from magma recharge), but could also be caused by less efficient outgassing through the lava lake as it fills.

Discussion

Halema‘uma‘u magma mass balance

Maintaining a persistent lava lake for a decade requires a remarkable thermal and mechanical balance. Relatively constant magma supply from depth is needed to drive continuous convection, but supply must be countered by sufficient outflux to prevent conditions leading to violent eruption. Ground deformation and VLP seismicity provide a quasi-continuous probe of magma properties that facilitates interrogation of the multiscale processes maintaining (and modulating) this balance within the Halema‘uma‘u reservoir during an extended eruption.

In general, magma reservoir pressure can change even without any magma input due to gas exsolution and (to a lesser extent) crystallization. However, since the low-viscosity mafic melt and open-vent structure of Halema‘uma‘u facilitates gas escape, reservoir pressurization has been inferred to reflect accumulation of melt either due to changes in influx (e.g., recharge from the South Caldera reservoir or deeper storage regions) or outflux (e.g., to the East Rift Zone) (*4, 44*). For example, the inferred causes of the May 2015 summit intrusion, the 2018 eruption, and the prevalent hours-days long “deflation-inflation” summit deformation events are: months of increased magma influx (*4, 6, 27*), months of reduced magma outflux (*45*), and transient restrictions of magma influx or outflux (*6, 8, 38*). However, the general controls on magma mass balance over days-years are unknown. The 60 and 130 day period spectral peaks in Halema‘uma‘u reservoir pressure (also apparent in temperature, ΔX, and X^{avg}) (Fig. 4) may indicate dominant timescales for such changes in influx-outflux (*4*). Quasi-periodic deformation and/or eruptive activity on similar timescales has also been observed at other volcanoes (*46,47*).

We might expect magma recharge to increase conduit temperature, although this would depend on the temperature and influx of recharging magma, and also its path through the $\sim$4 km^3 of near-liquidus magma in the Halema‘uma‘u reservoir (*11, 24*). The inferred 2011-2012 average magma supply rate of $\sim 10^9$ kg/day (*34*) would permit complete exchange with the $\sim 10^{10}$ kg of magma in the conduit and lava lake over a week. However, if this injected magma were uniformly mixed with the magma in the reservoir ($\sim 10^{13}$ kg assuming a density of 2500 kg/m^3) at a 100 °C temperature difference, the mixture temperature would only increase by $\sim$0.01 °C/day (neglecting latent heat and outflow). Given the poor coherence between Halema‘uma‘u reservoir pressure (or lava lake elevation) and temperature (Fig. 4), we expect that melt injected into the Halema‘uma‘u reservoir generally either was not appreciably hotter than existing magma and/or was not directly routed to the conduit.

One prominent exception that could exemplify an influx of hotter melt from depth is the persistent $\sim$100 °C increase in temperature six months before the Mar 2011 Kamoamoa fissure eruption. There was no corresponding increase in volatile mass fractions, potentially due to deeper separation and upward flux of volatiles over the preceding months of elevated volatile mass fractions. Interestingly, temperature then dropped by $\sim$100 °C in the months leading up to the eruption, which we expect relates to lava lake downwelling rather than magma influx/outflux, as discussed in the next section. Another potential example of hot melt influx is the $\sim$90 °C increase in temperature between the May 2012 slow-slip event on Kīlauea's south flank décollement and the Oct 2012 intrusion, although there was also no corresponding increase in volatile mass fractions. The temperature increase supports previous suggestions that slow-slip events are linked to magmatism (*48*), although we do not see similar temperature increases immediately following the 2010 or 2015 slow-slip events.

It is less obvious what changes in magma properties might be expected from decreased magma outflux, so we use the 2018 eruption as a case study. The months of pressurization preceding the eruption are accompanied by a decrease in magma temperature and increase in X^{avg}, but these do not clearly stand out from the background variation over the preceding year (Fig. 3). The lack of clear changes in magma properties is consistent with the idea that the 2018 eruption was triggered by decreasing outflux rather than by recharge (*45*) and, by extension, suggests that outflux does not necessarily drive significant changes in shallow magma properties. The May 2014 and May 2015 intrusions were also preceded by a month of Halemaʻumaʻu reservoir pressurization without other clearly associated changes in the summit magma system. The lack of clear changes in magma properties would seem to suggest they were induced by decreased magma outflux, although at least in 2015 changes in East Rift Zone lava effusion were not apparent (*4, 6, 27*). The Jun 2014 and May 2016 PuʻuʻŌʻō vent openings were not preceded by significant pressurization of the shallow summit magma system, suggesting they were not primarily caused by increased melt flux from the summit but rather by processes along the rift zone.

Shallow magma dynamics

Our results illuminate shallow fluid dynamic processes underlying a persistent lava lake. Observed covariation of parameters in our inversions suggest that volatile mass fraction and temperature in the conduit and lava lake vary in ways not always directly related to Halemaʻumaʻu reservoir magma influx/outflux. We infer that such variation occurs due to unsteady exchange flow between the conduit and Halemaʻumaʻu reservoir (*49*), as well as due to changing convective efficiency in the lava lake and/or surface crust dynamics (which influence the outgassing rate and efficiency of heat loss to the atmosphere and host rock) (*4, 50*).

The negative correlation on timescales of months or less between X^{avg} and temperature (Fig. 4, S6) likely reflects such dynamics, since relatively poor coherence with Halemaʻumaʻu reservoir pressure (or lava lake elevation) indicates neither X^{avg} or temperature are primarily driven by magma mass balance. Simple thermal arguments suggest likely causes of temperature variation. Atmospheric heat exchange at the lake surface will be dominated by radiative heat flux $\phi_r = A\epsilon\sigma(T_{surf}^4 - T_{atm}^4)$, where ϕ_r is $\sim$1 GW for lake surface area $A \approx 10^4$ m^2, thermal emissivity $\epsilon \approx 0.8$, Stefan-Boltzmann constant $\sigma = 5.7\times10^{-8}$ Wm^{-2}K^{-4}, and average surface temperature $T_s \approx 700$ °C (*50*). Heat flux to the host rock depends upon hydrothermal circulation, but can be approximated with an effective thermal conductivity $\phi_c = k_e \Delta T/\Delta L$, where ϕ_c is 10-1000 W/m^2 for k_e of 2-20 Wm^{-1}C^{-1} (*51*) and temperature gradient $\Delta T/\Delta L$ of 10-100 °C/m (*52*). Total heat transfer rate Φ from the conduit and lake (surface area $\sim$10^5 m^2) and from the Halemaʻumaʻu reservoir (surface area $\sim$10^7 m^2) is 1-100 MW and 0.1-10 GW, respectively. Neglecting latent heat, average temperature of a magma mass M will decrease as $dT/dt = \Phi/(c_p M)$. For specific heat $c_p \approx 1000$ Jkg^{-1}K^{-1}, average temperature of the $\sim$10^{10} kg of magma in the conduit and lake could decrease by $\sim$10 °C/day, whereas average temperature of the $\sim$10^{13} kg of magma in the Halemaʻumaʻu reservoir would only decrease by $\sim$0.01-1 °C/month. We thus expect the prevalent temperature drops of 100 °C or more that occur over days-weeks represent downwelling of magma that cooled in the upper lava lake. Episodic downwelling suggests episodically decoupled convection cells in the lava lake, rather than a convective regime that settles persistently into one of the configurations previously proposed (*6,53*). This mechanism likely explains the $\sim$100 °C temperature drop preceding the Mar 2011 Kamoamoa fissure eruption, where a changing convective regime is perhaps related to the rapidly filling lava lake and/or high short-term (hours-days) variability in lava lake elevation during this time. In some other cases rapid lava lake draining might also induce downwelling of cool magma. This downwelling could explain the days-long temperature decreases accompanying the Oct 2012 and May 2014 intrusions, although if so it is interesting that the 2015 intrusion did not cause a temperature drop.

An evolving magma plumbing system geometry

Given a consistent open hydraulic connection between the Halemaʻumaʻu reservoir and lava lake, the weakening coherence between them over years or longer (Fig. 4) could represent either changes in the magma column density or in the relation between reservoir pressure and ground deformation (a function of geometry and poro-visco-elastic rock properties). Our fixed geometry inversions test the former and show that for a range of feasible fixed parameter values (Fig. S5) very high values of X^{avg} and/or ΔX are required over some portion of the timeline (e.g., 2009 through mid-2010 for reference parameters). These volatile contents would correspond to a foam in the upper conduit and lava lake with an average porosity in excess of 90%. Available constraints from gravity data (*12*) suggest average porosity in the lava lake of only up to 70%, so the higher values inferred at early times are likely unrealistic. We thus expect subsurface magma plumbing system geometry evolved over time, which could also contribute to the weak coherence between inverted South Caldera and Halemaʻumaʻu reservoir pressures over long timescales (Fig. 4).

Changes in conduit length (reservoir-roof depth) of $\sim$10 m or changes in conduit radius of $\sim$1 m could measurably impact VLP resonance period and quality factor at Kīlauea (Fig. S5). Such changes might occur gradually due to processes such as viscous deformation of the host rock, thermal/mechanical erosion, or crystallization. Geometry could also change abruptly due to host rock failure or opening/closing of hydraulically connected dikes/sills. To fit the low VLP periods in 2009-2010 with realistic volatile contents, a $\sim$100 m higher reservoir roof elevation (510 instead of 410 m ASL, which is within estimated uncertainty (*11*)) and/or strongly tapered conduit (e.g., top radius < 5 m and bottom radius > 15 m) is required (Fig. S9). It is unlikely that the roof of an ellipsoidal reservoir would have grown downward this much over year timescales due to crystallization, so it may have been shallower throughout the eruption. In this case the drastic change in VLP periods over the early part of the eruption likely represent an evolving conduit geometry due to some combination of a widening upper conduit and a change in conduit length due to a changing dip angle and reservoir attachment depth. A shallow dike/sill above the main Halemaʻumaʻu reservoir could have also impacted the resonance (*54*); this would be potentially consistent with some seismic inversions (*21, 33*) but such additional source complexity is not needed according to other seismic and geodetic inversions (*7, 9, 11*).

Towards a new generation of volcano monitoring

Resolving the dynamics of subsurface magma transport is a grand challenge that dictates hazard forecasting efficacy as well as connections between active volcanic processes and the geologic record. Inferring relative changes in magma properties over days to months by identifying the fluid origin of Very-Long-Period seismic events represents a concrete step towards unifying the inversion of geophysical and geochemical data. In particular, we have resolved temperature changes of over 100 °C that likely reflect both convective overturns and magma recharge. We have also resolved stratified volatile profiles that represent a highly disequilibrium outgassing regime. Volatile contents vary by over 1 wt% on timescales from days to months, revealing an unsteady shallow volatile mass balance. We have also inferred an evolving magma system geometry, highlighting the need to develop models and data sets that can deconvolve changing fluid properties from changing transport pathways.

Incorporating additional data would yield even more precise constraints on multiphase magma properties and their depth variation. For example, continuous gravity data would provide independent constraints on magma density in the lake. Video of lake surface oscillations could independently constrain vertical motions of the lake and triggering mechanisms of VLP events. Additionally, surface gas emission data could constrain volatile stratification and outgassing/convective regimes if combined with models for gas flux through the magma column.

Similar Very-Long-Period events have been detected at Vanuatu and Erebus volcanoes (*55, 56*) and are expected at open-vent volcanoes generally (*20*), suggesting this type of analysis could be adapted to improve near real time monitoring at other eruptions. These data will inform basic volcano science and lead to better understanding of physical controls on volcanic eruptions.

Materials and Methods

GNSS inversions

To obtain time series of pressure change in the Halemaʻumaʻu reservoir, we must consider other known sources of ground deformation at Kīlauea summit: the South Caldera reservoir (*7, 8*), 2015 intrusion (*27*), and steady slip along the south flank décollement (*57*) (Fig. S3).

We assume a temporally fixed geometry for the three magma reservoirs (Fig. 1, supplementary text), but constrain the 2015 intrusion to be an active deformation source only over May 13-17 (*27*). We adopt the 2 km deep 4 km^3 ellipsoidal Halema‘uma‘u reservoir geometry and 3 GPa rock shear modulus from (*11*), consistent with other studies (*7, 9, 10, 58, 59*). We assume a horizontal centroid location of the South Caldera reservoir based on inversions of (*60*); depth and geometry are less well constrained so we choose a reference 20 km^3 sphere centered 4 km deep and test different values based on published ranges (*7, 10, 58*). We fix the 2015 intrusion geometry following (*27*).

Reservoir pressures are found using linear least square inversions (supplementary text) of daily average surface position solutions from Nevada Geodetic Laboratory (*61*) for GNSS stations within a few km of the reservoirs (Fig. 1), corrected for steady background south flank slip with the multi-component dislocation model of (*57*) (Fig. S3, S4). We use an approximate solution for deformation associated with a pressurized ellipsoid in an elastic half space (*62*) for each of the three magma bodies.

Conduit-reservoir magma oscillation model

We model VLP seismic events as small amplitude, isothermal and incompressible oscillatory magma flow within a lava lake-conduit-reservoir system. The model is extended from (*20*) to include inertial effects in the lava lake and experimentally constrained models for multiphase magma properties (supplementary text). We consider an inclined radially symmetric magma column encompassing the lava lake and conduit, underlain by a reservoir within elastic rocks (Fig. 1).

The magma column prior to VLP events is assumed magmastatic, justified because fluid particle velocities associated with resonance are larger than background exchange flow (*20*). During VLPs, viscous drag is determined from shear stress at the magma column wall where a no-slip velocity condition is enforced. With z and r distance parallel and perpendicular to the magma column axis (a function of conduit dip from horizontal θ), linearized conservation of momentum (primed variables) around a background state (bars) is

$$\frac{d\langle v'\rangle}{dt}\bar{\rho} = \langle u'\rangle \sin(\theta)\frac{d\bar{\rho}}{dz}g - \sin(\theta)\frac{\partial p'}{\partial z} + \frac{2\mu}{R}\left.\frac{\partial v'}{\partial r}\right]_R . \tag{1}$$

Here $\langle u'\rangle$ is cross-sectionally averaged conduit-parallel fluid particle displacement (so the orientation of $\langle u'\rangle$ is a function of θ), v' is conduit-parallel fluid particle velocity, $\langle v'\rangle$ is cross-sectionally averaged v' (the time derivative of $\langle u'\rangle$), ρ is magma density, p' is pressure perturbation, μ is dynamic viscosity, and R is conduit radius. Conservation of mass is $\langle u'\rangle = \langle u'_0\rangle R_0^2/R^2$, where subscript 0 indicates evaluation at the bottom of the magma column (Fig. 1).

We assume equilibrium joint solubility of CO_2 and H_2O in Halema‘uma‘u composition melts (*13*) as a function of pressure and gas composition (*25*) (supplementary text, Fig. S2). We neglect other volatile species as they have generally lower concentrations and/or poorly constrained solubility at Kīlauea (*13, 43*). We assume ideal gas behavior, and consider melt density a function of pressure, temperature, and composition (*29*). Melt viscosity $\mu_l(z)$ is assumed to be a function of temperature and dissolved H_2O (*31*). The impact of bubbles on apparent magma viscosity depends upon the magnitude of capillary forces (*30*). For expected strain rates of $\sim 10^{-1}$ s^{-1} associated with slow exchange flow in the conduit, bubbles less than $\sim$10 cm across will increase apparent viscosity approximately according to $\mu = \mu_l/(1-\bar{\phi})$ (Fig. S2), where $\bar{\phi}(z)$ is background magma porosity (*30*).

For conduit-reservoir resonance pressure at the base of the magma column is (*20*) $P_0' = -\pi R_0^2 \langle u_0' \rangle \sin(\theta_0)/C_r$, where C_r is the total storativity of the reservoir (reservoir volume change per unit pressure increase). The Halema'uma'u reservoir assumed here corresponds to a 'buoyancy-dominated' limit where reservoir pressure changes have a negligible effect on the magma column during VLPs (supplementary text) (*9*). Pressure at the top of the magma column is $P_H' = P_{ex} + \langle u_H' \rangle \sin(\theta_H)\bar{\rho}_H g$, where subscript H indicates evaluation at the top of the magma column and $P_{ex}(t)$ is external forcing (Fig. 1). This system is equivalent to a driven harmonic oscillator with frequency-dependent damping, and exhibits exponentially decaying oscillations in response to an impulsive forcing (Fig. S1). We find the resonant period and quality factor by solving numerically for the free response of the system (supplementary text).

VLP seismic event inversions

We assume a temporally fixed magma plumbing system geometry, except for lava lake radius and surface elevation which are interpolated from measurements (*4, 32*) (supplementary text). We choose reference fixed parameters based on previous constraints where available. Where minimal constraints are available, we test a range of values and select combinations that produce feasible inversion results over most of the timeline, as detailed in the supplementary text. We approximate the lava lake and conduit as cylinders, with a reference conduit radius of 15 m and conduit dip of 90 degrees from horizontal (Fig. 1, Table S1).

We conduct inversions using the conduit-reservoir resonance model for the three free parameters (temperature, X^{avg}, and ΔX) from the three target values for each VLP seismic event: conduit bottom (Halema'uma'u reservoir top) pressure, resonance period, and resonance quality factor (Fig. 2). We use an iterative nonlinear trust-region-reflective solver to find the combination of free parameter values that minimizes misfit E

$$E = \frac{|\omega - \omega^*|}{\omega^*} + \frac{|Q - Q^*|}{Q^*} + \frac{|\bar{P}_0 - \bar{P}_0^*|}{\bar{P}_0^*} \tag{2}$$

where vertical bars indicate absolute value, asterisks indicates observed/target values, Q is resonance quality factor, ω is resonance angular frequency, and $\bar{P}_0$ is magmastatic pressure at the bottom of the conduit (top of the reservoir). To prevent unfeasible solutions, we impose bounds on the search space such that volatile mass fraction at all depths is between 0-7 wt% and temperature is between 900-1600 °C. In most cases there is an exact solution ($E = 0$), although for some VLP events (e.g., in 2009 and early 2010) exact solutions do not exist for the reference parameters and the solver will find a local minimum instead. Grid searches indicate that the misfit spaces are convex, so the solver is finding unique global minima and/or unique exact solutions. Time-series analysis methods used to interpret inversions are detailed in the supplementary text.

References

1. M. Garcia, A. Pietruszka, M. Norman, M. Rhodes, *Chemical Geology* **581**, 120391 (2021).
2. J. Pallister, S. R. McNutt, *The Encyclopedia of Volcanoes* (Elsevier, 2015), pp. 1151–1171.
3. M. Manga, *et al.*, *Volcanic eruptions and their repose, unrest, precursors, and timing* (National Academies, 2017).
4. M. Patrick, D. Swanson, T. Orr, *Bulletin of Volcanology* **81**, 13 (2019).
5. C. Neal, *et al.*, *Science* **363**, 367 (2019).
6. M. P. Poland, A. Miklius, I. A. Johanson, K. R. Anderson, *U.S. Geological Survey Professional Paper 1867* (2021).
7. M. P. Poland, A. Miklius, E. K. Montgomery-Brown, *U.S. Geological Survey Professional Paper 1801-5* pp. 179–234 (2014).
8. A. Anderson, J. Foster, N. Frazer, *Journal of Volcanology and Geothermal Research* **397**, 106832 (2020).
9. C. Liang, J. Crozier, L. Karlstrom, E. Dunham, *Journal of Geophysical Research: Solid Earth* **125**, e2019JB017456 (2020).
10. T. Wang, Y. Zheng, F. Pulvirenti, P. Segall, *Journal of Geophysical Research: Solid Earth* **126**, e2021JB021803 (2021).
11. K. Anderson, *et al.*, *Science* **366**, eaaz1822 (2019).
12. M. Poland, D. Carbone, *Journal of Geophysical Research: Solid Earth* **121**, 5477 (2016).
13. M. Edmonds, *et al.*, *Geochimica et Cosmochimica Acta* **123**, 284 (2013).
14. A. H. Lerner, *et al.*, *Bulletin of Volcanology* **83**, 43 (2021).
15. T. Elias, A. J. Sutton, *U.S. Geological Survey Open-File Report 2012-1107* p. 25 p (2012).
16. T. Elias, C. Kern, K. Horton, A. Sutton, H. Garbeil, *Frontiers in Earth Science* **6**, 214 (2018).
17. S. Vergniolle, C. Jaupart, *Journal of Geophysical Research* **95**, 2793 (1990).

18. B. Chouet, R. Matoza, *Journal of Volcanology and Geothermal Research* **252**, 108 (2013).

19. L. Karlstrom, E. M. Dunham, *Journal of Fluid Mechanics* **797**, 431 (2016).

20. C. Liang, L. Karlstrom, E. Dunham, *Journal of Geophysical Research: Solid Earth* **125**, e2019JB017437 (2020).

21. B. Chouet, P. Dawson, *Journal of Geophysical Research: Solid Earth* **118**, 5352 (2013).

22. J. Crozier, L. Karlstrom, *Journal of Geophysical Research: Solid Earth* **126**, e2020JB020837 (2021).

23. P. Dawson, B. Chouet, *Journal of Volcanology and Geothermal Research* **278-279**, 59 (2014).

24. C. Gansecki, *et al.*, *Science* **366**, eaaz0147 (2019).

25. G. Iacono-Marziano, Y. Morizet, E. Le Trong, F. Gaillard, *Geochimica et Cosmochimica Acta* **97**, 1 (2012).

26. Materials and methods are available as supplementary materials at the science website.

27. M. J. Bemelmans, E. de Zeeuw-van Dalfsen, M. P. Poland, I. A. Johanson, *Journal of Volcanology and Geothermal Research* **415**, 107250 (2021).

28. A. C. Fowler, M. Robinson, *Journal of Volcanology and Geothermal Research* **356**, 141 (2018).

29. R. A. Lange, I. S. E. Carmichael, *Geochimica et Cosmochimica Acta* **51**, 2931 (1987).

30. E. W. Llewellin, M. Manga, *Journal of Volcanology and Geothermal Research* **143**, 205 (2005).

31. D. Giordano, J. K. Russell, D. B. Dingwell, *Earth and Planetary Science Letters* **271**, 123 (2008).

32. M. Patrick, D. Swanson, T. Orr, F. Younger, W. Tollett, Elevation of the lava lake in Halema'uma'u crater, Kilauea Volcano, from 2009 to 2018 (2022).

33. B. Chouet, P. Dawson, M. James, S. Lane, *Journal of Geophysical Research* **115**, B09311 (2010).

34. K. Anderson, M. Poland, *Earth and Planetary Science Letters* **447**, 161 (2016).

35. M. DiBenedetto, Z. Qin, J. Suckale, *Science Advances* **6** (2020).

36. M. Edmonds, I. Sides, J. Maclennan, *Hawaiian Volcanoes* (American Geophysical Union, 2015), chap. 15, pp. 323–349.

37. M. Poland, D. Carbone, *Geophysical Research Letters* **45**, 2319 (2018).

38. K. Anderson, M. Poland, J. Johnson, A. Miklius, *Hawaiian Volcanoes* (American Geophysical Union, 2015), chap. 11, pp. 229–250.

39. M. Shirzaei, T. R. Walter, R. Bürgmann, *Geophysical Research Letters* **40** (2013).

40. D. Elsworth, G. Mattioli, J. Taron, B. Voight, R. Herd, *Science* **322** (2008).

41. M. Aloisi, *et al.*, *Geophysical Research Letters* **38** (2011).

42. K. Anderson, M. Poland, *Nature Geoscience* **10**, 704 (2017).

43. A. Burgisser, M. Alletti, B. Scaillet, *Computers & Geosciences* **79**, 1 (2015).

44. D. Dzurisin, M. Poland, *Field Volcanology: A Tribute to the Distinguished Career of Don Swanson* (Geological Society of America, 2019), vol. 538, pp. 275–295.

45. M. Patrick, *et al.*, *Nature Communications* **11**, 5646 (2020).

46. S. Hautmann, *et al.*, *Tectonophysics* **471** (2009).

47. A. Toombs, G. Wadge, *Journal of Volcanology and Geothermal Research* **245-246** (2012).

48. E. Montgomery-brown, M. Poland, A. Miklius, *Hawaiian Volcanoes: From Source to Surface* (Blackwell, 2015), vol. 208, pp. 269–288.

49. J. Suckale, Z. Qin, D. Picchi, T. Keller, I. Battiato, *Journal of Fluid Mechanics* **850** (2018).

50. J. Thompson, M. Ramsey, *Journal of Volcanology and Geothermal Research* **408**, 107077 (2020).

51. H. Schmeling, G. Marquart, *Geophysical Journal International* **197**, 645 (2014).

52. P. Hsieh, S. Ingebritsen, *Journal of Geophysical Research: Solid Earth* **124**, 1498 (2019).

53. M. Patrick, T. Orr, D. Swanson, E. Lev, *Journal of Volcanology and Geothermal Research* **328**, 247 (2016).

54. M. McQuillan, L. Karlstrom, *Journal of Glaciology* **1**, 1 (2021).

55. R. Aster, *Journal of Geophysical Research Solid Earth* **108** (2003).

56. T. Shreve, *et al.*, *Scientific Reports* **9**, 18868 (2019).

57. S. Owen, *et al.*, *Journal of Geophysical Research: Solid Earth* **105**, 18983 (2000).

58. S. Baker, F. Amelung, *Journal of Geophysical Research: Solid Earth* **117**, B12406 (2012).

59. A. Roman, P. Lundgren, *Nature* **592**, 392 (2021).

60. M. Poland, A. Miklius, A. Jeff Sutton, C. Thornber, *Nature Geoscience* **5**, 295 (2012).

61. G. Blewitt, W. Hammond, C. Kreemer, *Eos* **99** (2018).

62. M. Battaglia, P. F. Cervelli, J. R. Murray, *Journal of Volcanology and Geothermal Research* **254**, 1 (2013).

63. P. Segall, *Earthquake and volcano deformation* (Princeton University Press, 2010).

64. J. R. Womersley, *The Journal of Physiology* **127**, 553 (1955).

65. Y. Zhang, Z. Xu, M. Zhu, H. Wang, *Reviews of Geophysics* **45**, RG4004 (2007).

66. M. T. Mangan, K. V. Cashman, D. A. Swanson, *U.S. Geological Survey Professional Paper 1801-8* pp. 323–354 (2014).

67. H. Mader, E. Llewellin, S. Mueller, *Journal of Volcanology and Geothermal Research* **257**, 135 (2013).

68. J. Suckale, B. H. Hager, L. T. Elkins-Tanton, J. C. Nave, *Journal of Geophysical Research: Solid Earth* **115**, 7410 (2010).

69. J. E. Gardner, R. A. Ketcham, G. Moore, *Journal of Volcanology and Geothermal Research* **267**, 68 (2013).

70. C. A. Williams, G. Wadge, *Journal of Geophysical Research: Solid Earth* **105**, 8103 (2000).

71. A. Grinsted, J. C. Moore, S. Jevrejeva, *Nonlinear Processes in Geophysics* **11**, 561 (2004).

Acknowledgments

We thank the Hawaiian Volcano Observatory and Hawaiʻi Volcanoes National Park. We thank US Geological Survey staff including Kyle Anderson, Emily Montgomery-Brown, Matt Patrick, Kendra Lynn, Ingrid Johanson, and Phillip Dawson for data and discussion of Kīlauea. We thank Chao Liang and Eric Dunham for discussion of VLP events. We thank editor Blair Schoene as well as Matt Haney and two anonymous reviewers for thorough and constructive feedback. Any use of trade, firm, or product names is for descriptive purposes only and does not imply endorsement by the U.S. Government.

Funding

National Science Foundation grant EAR-2036980 (LK)

Author contributions

Conceptualization: JC, LK

Methodology: JC

Writing: JC, LK

Competing interests

Authors declare that they have no competing interests

Data and materials availability

All data and codes are available at https://bitbucket.org/crozierjosh1/vlp_inversion_codes or https://doi.org/10.7910/DVN/1NNZTJ. GNSS data can also be found at http://geodesy.unr.edu/, the VLP seismic event catalog can also be found at https://doi.org/10.7910/DVN/2UGFKE, and lava lake data can be found at https://doi.org/10.5066/P9ULRPMM.

Supplementary Materials

Materials and Methods

Supplementary Text

Figs. S1 to S10

Table S1

References *(63-71)*

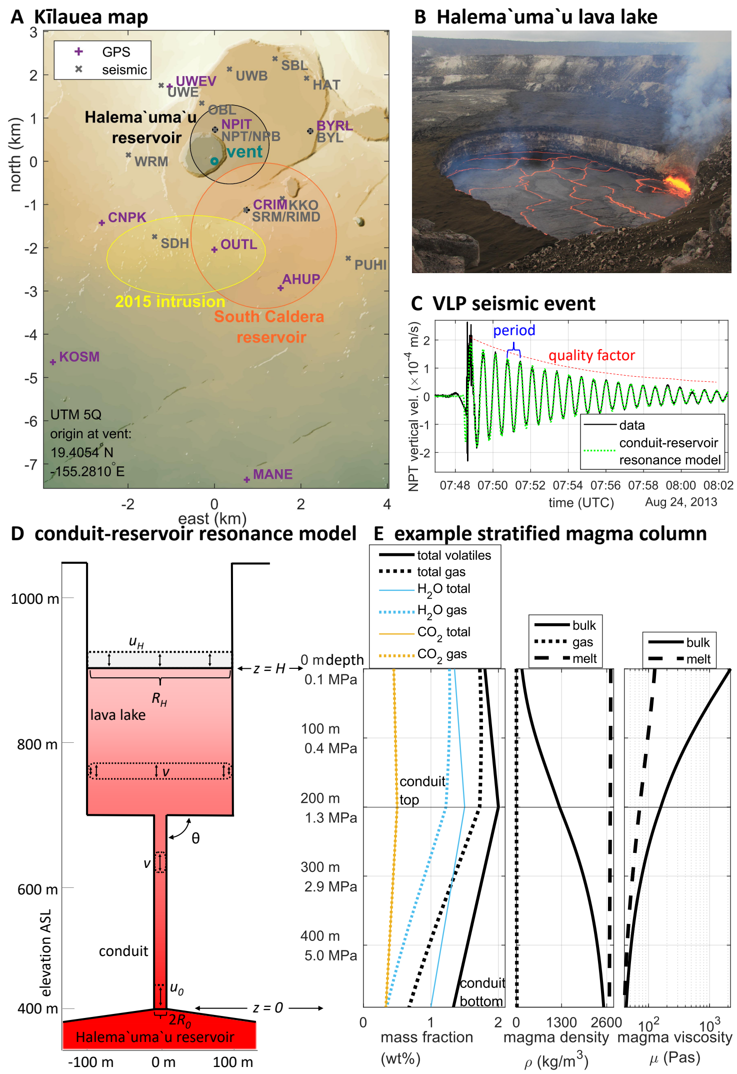

Fig. 1. Kīlauea map and magma dynamics model. (**A**) Map including the Halema'uma'u vent, inferred shallow magma storage zones, GNSS stations, and seismometers used in the VLP catalog (*22*). (**B**) Typical lava lake activity on Feb 13, 2017 (USGS). (**C**) Seismic waveform from a VLP conduit-reservoir resonance event along with a model solution for reference fixed parameter inversion results forced with a Gaussian pressure perturbation (Fig. S1). (**D**) Conduit-reservoir resonance model with approximate 2018 magma system geometry; black arrows illustrate vertical sloshing of the stratified magma column. (**E**) Magmastatic depth profiles from piecewise linear total (dissolved plus exsolved) volatile mass fractions at a uniform temperature of 1200 °C.

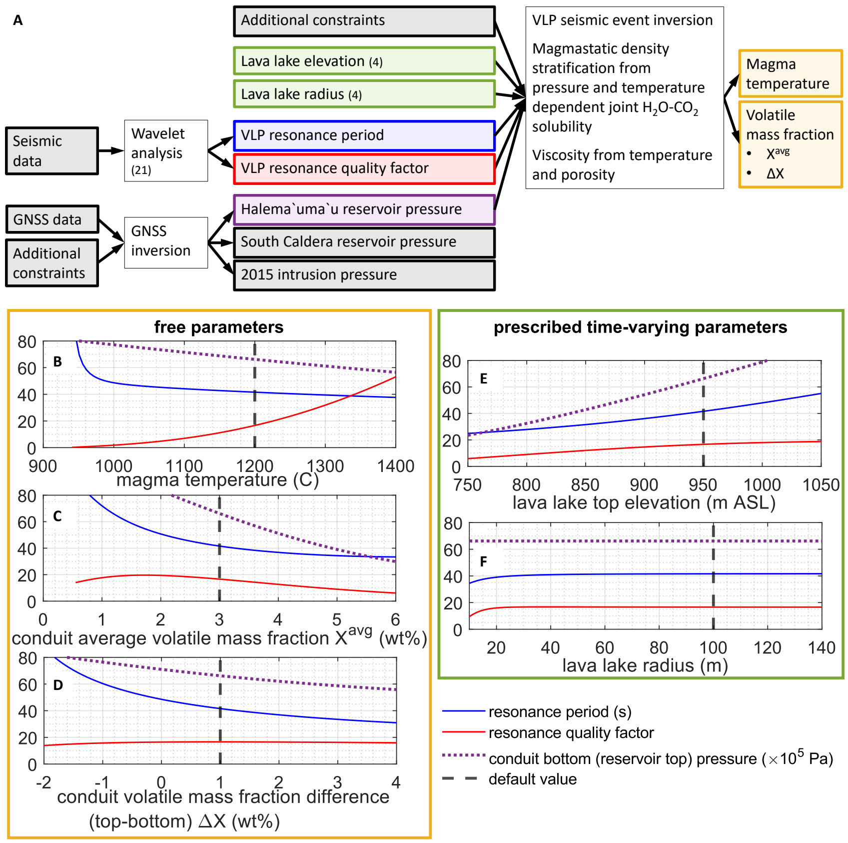

Fig. 2. Inversion approach. (**A**) Simplified flowchart of methods and data input/output. Additional constraints on GNSS inversions are from previous geodetic studies (*11, 27, 57, 60*). Additional constraints on VLP magma resonance inversions are from previous modeling (*9*), gravity data (*37*), and geochemical (gas and ejecta) data (*13, 16, 24, 36*). (**B-F**) Conduit-reservoir resonance period and quality factor, plus conduit bottom pressure, as a function of the parameters varied to fit Kīlauea VLP seismic and geodetic data. Variation in lava lake elevation and (assumed uniform) radius are prescribed from measurements (*4, 32*). Dashed black lines indicate default values used in the other plots.

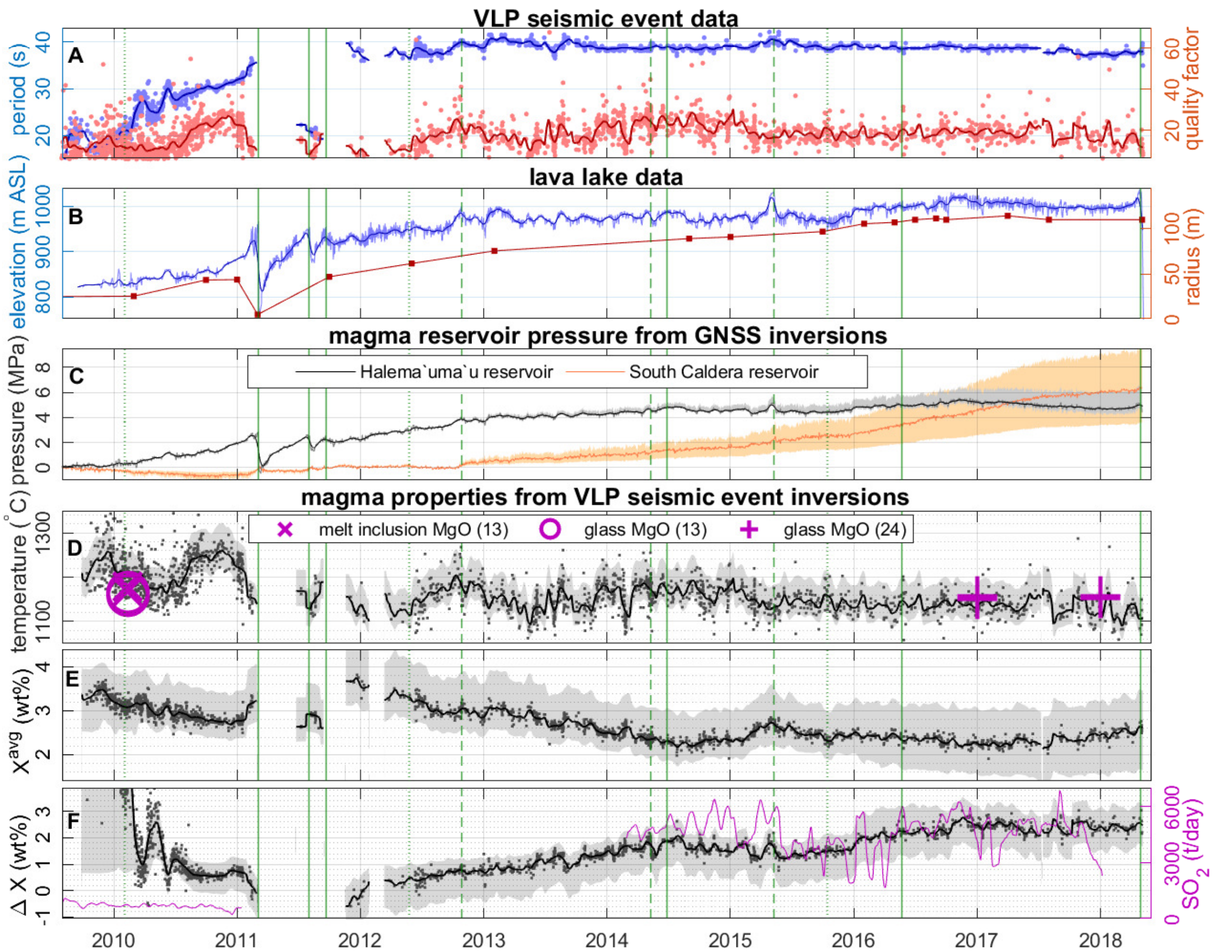

Fig. 3. Time series data and inversion results. Inverted relative changes in magma properties are from our reference fixed parameters (Fig. 1, Table S1). Dots represent individual VLP seismic events, bold lines are 30-day moving averages, while vertical green lines are East Rift Zone eruptions (solid), summit intrusions (dashed), and slow-slip events (dotted) (*4*). (**A**) VLP seismic event resonance period and quality factor (*22*). (**B**) Lava lake elevation and mean radius (*4, 32*) (**C**) GNSS inverted reservoir pressure changes, set to zero at the Mar 7, 2011 lava lake draining. Shaded areas indicate possible variation with different South Caldera reservoir geometries tested (supplementary text). (**D**) Inverted conduit magma temperature, with MgO thermometry for comparison (*13, 24*). The shaded area indicates possible variation with all fixed model parameter values tested (supplementary text). (**E, F**) Inverted conduit total volatile contents, with 30-day moving average SO_2 emissions for comparison (*15, 16*) and possible variation shown in shaded areas. Values from 2009-early 2010 are unreliable due to exact solutions not being obtainable with the fixed parameters chosen.

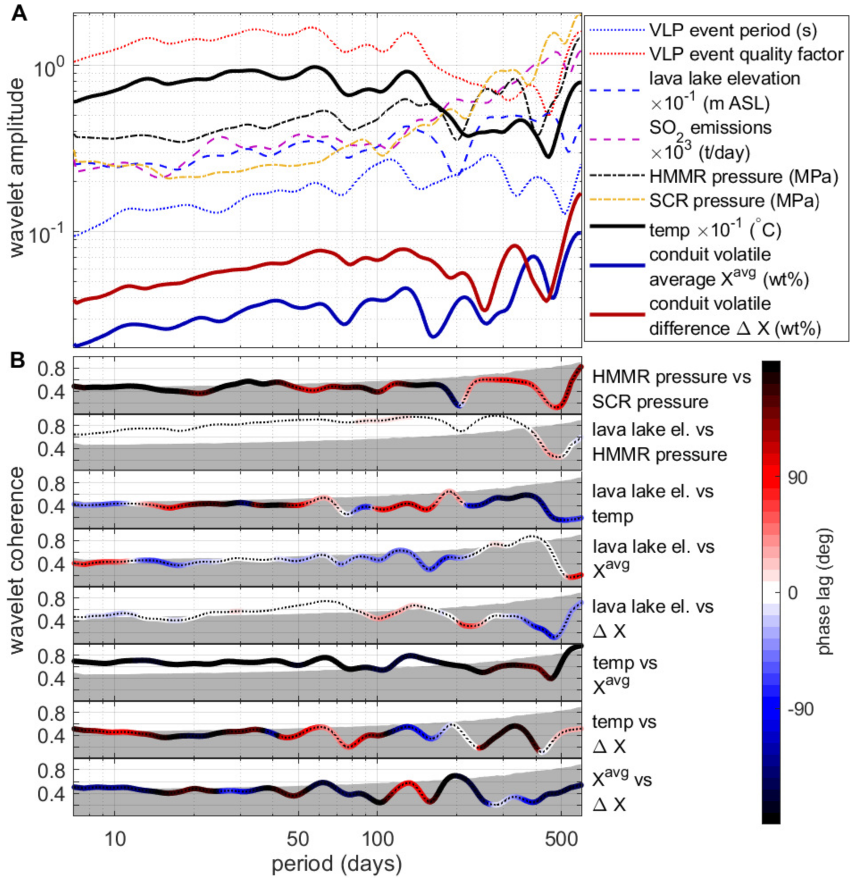

Fig. 4. Wavelet amplitude spectra and coherence. (**A**) Amplitude spectra of resonance properties (*22*), lava lake elevation (*4, 32*), SO_2 emissions (*15, 16*), GNSS inverted Halemaʻumaʻu (HMMR) and South Caldera (SCR) reservoir pressures, and VLP magma resonance inverted magma properties. (**B**) Magnitude squared coherence colored by phase lag. The gray area is beneath the 95% significance threshold. Positive phase lags indicate that the second variable trails the first. Data before Dec 2011 were excluded from this analysis.

Supplementary Material for

Evolving magma temperature and volatile contents over the 2008-2018 eruption of Kīlauea Volcano

Josh Crozier, Leif Karlstrom

Correspondence to: jcrozier@usgs.gov

Supplementary Text

Conduit-reservoir model description

We consider a magmatic system consisting of a slowly convecting, vertically stratified column of fluid underlain by a reservoir in an elastic halfspace and overlain by a lava lake. Our model domain extends from the bottom of the conduit (or top of the reservoir) to the surface of the lava lake. To model VLP events, we separate the transient flow associated with small perturbations to this system from background dynamics. To first approximation, wave-like disturbances are rapid compared to background exchange flow so it suffices to consider a magmastatic background state upon which small amplitude flow is superimposed (*20*). For sufficiently long period flow, we can neglect the compressibility of magma in the column and conduit wall elasticity. We adopt a coordinate system where z is the Cartesian direction parallel to the conduit/lava lake axis and r is the radial direction perpendicular to z, so the orientation of r and z is a function of conduit dip angle $\theta(z)$. Function arguments are omitted except where necessary. Linearized governing equations are derived for small amplitude uni-directional magma flow in this system using a perturbation approach,

$$[v(r,z,t), p(z,t), \rho(z,t)] = [0, \bar{p}(z), \bar{\rho}(z)] + [v'(r,z,t), p'(z,t), \rho'(z,t)], \tag{3}$$

where v is conduit-parallel fluid particle velocity (so the orientation of v is a function of conduit dip angle $\theta(z)$), p is pressure, ρ is magma density, overbar indicates background values, and prime indicates perturbations. We denote cross-sectional averaging as

$$\langle v\rangle(z,t) = \frac{2}{R^2}\int_0^R v(r,z,t)r\,dr \tag{4}$$

We also express motion in terms of cross-sectionally-averaged conduit-parallel fluid particle displacement $\langle u\rangle$,

$$\frac{d\langle u\rangle}{dt} = \langle v\rangle. \tag{5}$$

Magma density perturbation will result from advection of the background density profile

$$\rho = \langle u'\rangle \sin(\theta)\frac{d\bar{\rho}}{dz}. \tag{6}$$

Linearized conservation of momentum for perturbations is then given by

$$\frac{\partial v'}{\partial t}\bar{\rho} = \langle u'\rangle \sin(\theta)\frac{d\bar{\rho}}{dz}g - \sin(\theta)\frac{\partial p'}{\partial z} + \mu\frac{1}{r}\frac{\partial}{\partial r}\left(r\frac{\partial v'}{\partial r}\right) \tag{7}$$

where μ is magma viscosity and g is gravitational acceleration. We assume a zero slip boundary condition along the magma column (conduit/lava lake) wall at radius $R(z)$

$$v'(z, R(z), t) = 0. \tag{8}$$

Viscous drag force can be determined from the shear stress at the magma column wall, so cross-sectionally averaging Eq. 7 gives

$$\frac{d\langle v'\rangle}{dt}\bar{\rho} = \langle u'\rangle \sin(\theta)\frac{d\bar{\rho}}{dz}g - \sin(\theta)\frac{\partial p'}{\partial z} + \frac{2\mu}{R}\left.\frac{\partial v'}{\partial r}\right]_R. \tag{9}$$

Incompressible linearized cross-sectionally averaged conservation of mass is

$$\langle u'\rangle = \langle u'_0\rangle \frac{R_0^2}{R^2}, \tag{10}$$

where a zero subscript indicates evaluation at the bottom of the magma column (or top of the reservoir), e.g., $R_0 = R(z = 0)$, and subscript H indicates evaluation at the top of the magma column (or top of the lava lake).

We apply pressure perturbation boundary conditions at the top of the magma column and mass balance at the base. Neglecting fluid inertia and viscous dissipation in the reservoir due to long period forcing (*20*), linearized mass balance at the base of the magma column becomes a condition on basal pressure perturbation p'_0,

$$p'_0 = -\frac{\pi R_0^2 \langle u'_0\rangle}{C_r}\sin(\theta_0), \tag{11}$$

where C_r is the total storativity (injected magma volume per unit pressure increase) of the reservoir,

$$C_r = (\beta_m + \beta_r)V_r, \tag{12}$$

where V_r is reservoir volume, $\beta_m = \frac{1}{\rho}\frac{d\bar{\rho}_r}{dp_r}$ is effective magma compressibility in the reservoir, and $\beta_r = \frac{1}{V_r}\frac{dV_r}{dp_r}$ is the elastic reservoir compressibility. For a spherical reservoir $\beta_r = \frac{3}{4G}$, where G is the host rock elastic shear modulus (*63*). Linearized pressure perturbation at the top of the magma column p'_H is a function of external forcing pressure $P_{ex}(t)$ and the displaced magma mass at the free surface,

$$p'_H = P_{ex} + \langle u'_H\rangle \sin(\theta_H)\bar{\rho}_H g = p'_{ex} + \langle u'_0\rangle \sin(\theta_H)\frac{R_0^2}{R_H^2}\bar{\rho}_H g. \tag{13}$$

Integrating momentum (Eq. 9) in the z-direction over magma column height H and substituting in conservation of mass (Eq. 10) and the boundary conditions (Eq. 11 and 13) gives

$$\begin{aligned} &\frac{d^2\langle u'_0\rangle}{dt^2}R_0^2\int_0^H \frac{1}{\sin(\theta)}\frac{\bar{\rho}}{R^2}dz = \\ &\langle u'_0\rangle R_0^2\left(g\left(\int_0^H \frac{d\bar{\rho}}{dz}\frac{1}{R^2}dz - \bar{\rho}_H\frac{1}{R_H^2}\sin(\theta_H)\right) - \frac{\pi}{C_r}\sin\theta_0\right) + \int_0^H \frac{1}{\sin(\theta)}\frac{2\mu}{R}\left.\frac{\partial v'}{\partial r}\right]_R dz - P_{ex}. \end{aligned} \tag{14}$$

Conduit-reservoir model solution

We assume a periodic pressure gradient with angular frequency ω and amplitude f, to focus on the fundamental eigenmode of the system (the conduit-reservoir oscillation)

$$\frac{\partial p'}{\partial z} = f e^{i\omega t}. \tag{15}$$

Velocity can then be expressed analytically (*64*)

$$v' = \frac{f e^{i\omega t}}{i\omega\bar{\rho}}\left(1 - \frac{J_0\left(r\alpha\right)}{J_0\left(R\alpha\right)}\right), \tag{16}$$

where J_n is a Bessel function of the first kind and order n, and α is

$$\alpha = \sqrt{\frac{\omega\bar{\rho}}{\mu}}i^{3/2} \tag{17}$$

with $i = \sqrt{-1}$. Shear strain rate at the conduit/lava lake wall is then

$$\left.\frac{\partial v'}{\partial r}\right]_R = \frac{f e^{i\omega t}}{i\omega\bar{\rho}}\left(\frac{\alpha J_1\left(R\alpha\right)}{J_0\left(R\alpha\right)}\right), \tag{18}$$

and cross-sectionally averaged velocity $\langle v'\rangle$ is

$$\langle v'\rangle = \frac{f e^{i\omega t}}{i\omega\bar{\rho}}\left(1 - \frac{2}{R\alpha}\frac{J_1\left(R\alpha\right)}{J_0\left(R\alpha\right)}\right). \tag{19}$$

Substituting Eq. 19 into Eq. 18 and simplifying with the Bessel function recurrence relation $J_{n+1}(x) = \frac{2n}{x}J_n(x) - J_{n-1}(x)$ yields

$$\left.\frac{\partial v'}{\partial r}\right]_R = -\langle v'\rangle\frac{\alpha J_1\left(R\alpha\right)}{J_2\left(R\alpha\right)}. \tag{20}$$

Substituting Eq. 20, 5, and 10 into Eq. 14 and taking the real part finally gives

$$\begin{aligned}&\frac{d^2\langle u_0'\rangle}{dt^2}R_0^2\int_0^H \frac{1}{\sin(\theta)}\frac{\bar{\rho}}{R^2}dz = -P_{ex} \\ &+\langle u_0'\rangle R_0^2\left(g\left(\int_0^H \frac{d\bar{\rho}}{dz}\frac{1}{R^2}dz - \bar{\rho}_H\frac{1}{R_H^2}\sin(\theta_H)\right) - C_r^{-1}\pi\sin(\theta_0)\right) \\ &-\frac{d\langle u_0'\rangle}{dt}2R_0^2\mathbf{Re}\left[\int_0^H \frac{1}{\sin(\theta)}\frac{\mu}{R^3}\frac{\alpha J_1\left(R\alpha\right)}{J_2\left(R\alpha\right)}dz\right].\end{aligned} \tag{21}$$

This equation can be solved in the frequency domain for a given time function of P_{ex}. Examples of such solutions are given in Fig. 1 and Fig. S1.

To study the natural response of the conduit-reservoir oscillation we set the top external forcing pressure P_{ex} in Eq. 21 to zero (rendering forcing an initial condition), which gives a homogeneous damped harmonic oscillator equation

$$c_1 \frac{d^2 \langle u_0' \rangle}{dt^2} + c_2 \frac{d \langle u_0' \rangle}{dt} + c_3 \langle u_0' \rangle = 0. \tag{22}$$

In equation 22, c_1 scales the magnitude of the inertial term for the oscillator

$$c_1 = R_0^2 \int_0^H \frac{1}{\sin(\theta)} \frac{\bar{\rho}}{R^2} dz. \tag{23}$$

c_2 scales the viscous damping term

$$c_2 = 2R_0^2 \mathbf{Re} \left[\int_0^H \frac{1}{\sin(\theta)} \frac{\mu}{R^3} \frac{\alpha J_1(R\alpha)}{J_2(R\alpha)} dz \right], \tag{24}$$

and is a function of ω through α. c_3 scales the restoring force term (gravity and reservoir storativity),

$$c_3 = -R_0^2 \left(g \left(\int_0^H \frac{d\bar{\rho}}{dz} \frac{1}{R^2} dz - \frac{\bar{\rho}_H}{R_H^2} \sin(\theta_H) \right) - C_r^{-1} \pi \sin(\theta_0) \right). \tag{25}$$

Equation 22 has a general solution of the form

$$\langle u_0' \rangle (t) = \langle u_0' \rangle (t=0) e^{(\lambda + i\omega)t}, \tag{26}$$

with initial amplitude $\langle u_0' \rangle (t=0)$ set by the external pressure perturbation, temporal exponential decay rate constant

$$\lambda = \frac{c_2}{2c_1}, \tag{27}$$

and natural angular frequency

$$\omega = \sqrt{\frac{c_3}{c_1} - \left(\frac{c_2}{2c_1} \right)^2} = \sqrt{\omega_u^2 - \lambda^2}, \tag{28}$$

where undamped (inviscid) natural angular frequency $\omega_u = \sqrt{c_3/c_1}$. Since c_2 is a function of ω, Eq. 28 must be solved implicitly for ω, which then may be used to calculate λ from Eq. 27. Quality factor Q gives the ratio of energy stored to energy lost per oscillation cycle,

$$Q = \frac{\omega}{2\lambda}. \tag{29}$$

Conduit-reservoir model analytical solutions under simplified conditions

To gain more insight into these equations, we examine a simplified scenario that permits a concise analytical solution. We consider a vertical cylindrical magma column with uniform magma viscosity. We assume a linear magma density gradient between $\bar{\rho}_0$ and $\bar{\rho}_H$, alternately characterized by the vertically averaged density $\bar{\rho}_{avg} = (\bar{\rho}_H + \bar{\rho}_0)/2$ and the vertical density difference $\Delta\bar{\rho} = \bar{\rho}_H - \bar{\rho}_0$. We assume fully developed (Poiseuille) flow, which will provide an upper bound on viscous damping. This simplified scenario is similar to those considered in (*21*) and in the reduced conduit-reservoir eigenmode model of (*20*). In this scenario, the inertial scale factor reduces to

$$c_1 = H\bar{\rho}_{avg}, \tag{30}$$

the viscous damping scale factor reduces to Poiseuille drag

$$c_2 = H\frac{8\mu}{R^2}, \tag{31}$$

and the restoring force scale factor reduces to

$$c_3 = \bar{\rho}_0 g + \pi R^2 C_r^{-1}. \tag{32}$$

This yields an exponential decay rate of

$$\lambda = \frac{4\mu}{R^2\bar{\rho}_{avg}}, \tag{33}$$

a natural angular frequency of

$$\omega = \sqrt{\frac{g(\bar{\rho}_H - \Delta\bar{\rho}) + \pi R^2 C_r^{-1}}{H\bar{\rho}_{avg}} - \frac{16\mu^2}{R^4\bar{\rho}_{avg}^2}}, \tag{34}$$

and a quality factor of

$$Q = \frac{R^2\bar{\rho}_{avg}}{8\mu}\sqrt{\frac{g(\bar{\rho}_H - \Delta\bar{\rho}) + \pi R^2 C_r^{-1}}{H\bar{\rho}_{avg}} - \frac{16\mu^2}{R^4\bar{\rho}_{avg}^2}}. \tag{35}$$

The natural frequency of flow that is not fully developed, as will be the case during Kīlauea VLP events (*20*), will be between the natural frequency of fully developed flow and the undamped natural frequency (for which Q is not defined)

$$\omega_u = \sqrt{\frac{g(\bar{\rho}_H - \Delta\bar{\rho}) + \pi R^2 C_r^{-1}}{H\bar{\rho}_{avg}}}. \tag{36}$$

This simplified scenario permits an easy examination of the relative importance of restoring forces from gravity and reservoir storativity for the Kīlauea magma system geometry. The compressibility of the ellipsoidal Halema'uma'u reservoir geometry (*11*) is $\approx 2.5 \times 10^{-10}$ Pa^{-1}. Magma compressibility in the reservoir could range from 10^{-9} to 10^{-10} Pa^{-1} (*9*), from which Eq. 12 gives reservoir storativity of $\sim$1-5 m^3/Pa. For a conduit radius of 10-20 m (*9*), the reservoir storativity restoring force term in Eq. 32 will range from $\sim$60-300 N/m^3. The density difference across the conduit will likely be at least $\sim$1000 kg/m^3 (*9*). The gravity restoring force term in Eq. 32 will thus be at least $\sim$10^4 N/m^3, which is an order of magnitude larger than the reservoir storativity term. This is consistent with a similar analysis in (*20*).

Stratified magma properties

We prescribe piecewise linear depth profiles of magma temperature and total (dissolved plus exsolved) volatile contents, parameterized by their value at the bottom of the conduit, top of the conduit, and top of the lava lake. Density and viscosity are then calculated from these magma properties. We consider both CO_2 and H_2O, but do not explicitly treat other volatiles as their solubility and/or abundance is poorly constrained.

We approximate the background pressure profiles as magmastatic

$$\bar{p}(z) = \bar{P}_{atm} + \int_z^H \bar{\rho}(y) g dy, \tag{37}$$

where atmospheric pressure $\bar{P}_{atm} = 10^5$ Pa. Exchange flow could result in sub-magmastatic pressures (*28*), but this is not well constrained by data used here. Background bulk magma density is given by

$$\bar{\rho}(z) = \left(\frac{\bar{n}_g(z)}{\bar{\rho}_g(z)} + \frac{1 - \bar{n}_g(z)}{\bar{\rho}_l(z)} \right)^{-1}. \tag{38}$$

Where $\bar{n}_g$ is background gas mass fraction, $\bar{\rho}_l(z)$ is background gas density, and $\bar{\rho}_l(z)$ is background melt density. We calculate background melt density as a function of pressure, temperature, and composition using the model of (*29*) with average Halema'uma'u melt inclusion compositions from Table 7 in (*13*). We use the ideal gas law for background gas density:

$$\bar{\rho}_g(z) = \frac{\bar{p}(z)(\bar{n}_{H2O}(z) M_{H2O} + \bar{n}_{CO2}(z) M_{CO2})}{R_g T} \tag{39}$$

where $\bar{n}_m$ and M_m are the background exsolved gas mass fraction and molar mass of volatile species m, T is temperature, and R_g is the ideal gas constant.

To obtain exsolved gas mass fractions from total (dissolved plus exsolved) volatile mass fractions ($\bar{X}_{H2O}$, $\bar{X}_{CO2}$), we interpolate pre-computed volatile solubility from the model of (*25*). These give equilibrium H_2O and CO_2 solubility as a function of pressure and H_2O gas molar fraction, again using average Halema'uma'u melt inclusion compositions from (*13*). The accuracy of the chemical equilibrium assumption depends on the rate of magma ascent/descent relative to the rate of volatile diffusion in/out of bubbles. Estimated lava lake upwelling velocities of 0.15-0.3 m/s would yield magma ascent timescales in the lava lake on the order of hours (*53*). H_2O and CO_2 diffusivity are highly dependent on temperature and H_2O contents, but should be on the order of 10^{-9} to 10^{-11} m^2/s in the shallow Kīlauea magma system (*65*). This could correspond to chemical diffusion timescales from minutes to hours for typical bubble spacing of 10^{-5} to 10^{-3} m, and potentially longer in a regime dominated by isolated large bubble slugs (*66*).

We calculate melt viscosity $\mu_l(z)$ as a function of temperature and dissolved H_2O from the model of (*31*), again using the average Kīlauea glass composition from Table 7 in (*13*). Crystal contents (*67*) will increase bulk magma viscosity, but we neglect this given the relatively low crystal contents of Halemaʻumaʻu magma (*13*).

The effect bubbles have on bulk magma viscosity depends upon the flow regime (*30*). For oscillatory flows, this is governed by the dynamic capillary number, which is the ratio between the timescale over which bubbles relax to spherical shapes and the timescale over which changes in shear deformation occur: $C_d = \frac{\mu_l R_b}{\Gamma}\frac{\ddot{\epsilon}}{\dot{\epsilon}}$. For $C_d < 1$ bubbles will act as obstacles to flow and increase bulk magma viscosity, whereas for $C_d > 1$ bubbles will act as weak regions that deform preferentially and reduce bulk magma viscosity. Bubble radii R_b in effusive Hawaiian eruptions are on the order of 10^{-4} to 10^{-3} m, although there will likely be some lateral variability (*28*) and bubble slugs with widths up to the conduit width could occasionally be present (*33, 66*). However, very large bubble slugs would break-up and/or ascend on the order of minutes (*33,68*), and since Strombolian-type bubble bursts only occur intermittently (*33*) we assume that the conduit and lava lake are free of such large bubble slugs most of the time. We additionally note that if a bursting bubble slug triggers VLP resonance, that slug would not be present during the following resonance. Melt viscosity μ_l will be on the order of 10^1 to 10^2 Pa·s (*31*). Surface tension Γ will be on the order of 10^{-1} N/m (*69*). The mean strain rate ratio $\ddot{\epsilon}/\dot{\epsilon}$ for a sinusoidal velocity will be approximately $2\pi/T$, so on the order of 10^{-1} s^{-1} for these VLP events. C_d will then generally be on the order of 10^{-3} to 10^{-1}. We thus use the $C_d < 1$ capillary number model from (*30*) for background bulk magma viscosity,

$$\mu(z) = \frac{\mu_l(z)}{1 - \bar{\phi}(z)}, \tag{40}$$

where $\bar{\phi}(z)$ is background magma porosity, $\bar{\phi} = (\bar{\rho}_l - \bar{\rho})/(\bar{\rho}_l - \bar{\rho}_g)$. This relation becomes inaccurate as porosity approaches 1, such as in foam layers that might build up near the lava lake surface. However, we will show in the next section that the lava lake contributes negligibly to viscous damping during conduit-reservoir resonance.

Fig. S2 shows the effects of temperature and total (dissolved plus exsolved) volatile contents on magma properties.

Conduit-reservoir model exploration

We consider model parameters that are plausible for the Kīlauea magma plumbing system. We approximate the lava lake geometry as a vertical cylinder in all of our simulations. This is justified for the case of Kīlauea since at both times when the lava lake fully drained its geometry was roughly cylindrical (*4*), and we also found that using a conical frustum approximation to the lava lake geometry produced values of period and quality factor that differed from a cylindrical geometry by less than 1%. There are no direct constraints on conduit geometry except for limited observations from the times when the lava lake drained fully, where it appears that the top of the conduit is appreciably smaller than the base of the lava lake (*4*). Previous inversion by (*9*) of isolated Halemaʻumaʻu conduit-reservoir VLP events with a model similar to ours assuming a cylindrical conduit indicates a steeply dipping conduit with a most likely radius of 10-20 m. We consider conduit geometries consisting of either cylinders or conical frustums, and allow the conduit to dip at an angle θ from vertical.

While some previous VLP seismic inversions have inferred a source geometry of intersecting dikes (*21, 33*), an ellipsoidal reservoir is consistent with the collapse geometry observed in 2018 (*11*), with other geodetic inversions (*7, 10, 58, 59*), and previous work combining modeling with VLP seismic inversions (*9*). We thus adopt the ellipsoidal reservoir geometry and rock shear modulus found by (*11*) as our reference scenario. Simulations for our assumed Kīlauea magma system geometry verify that reservoir storativity has a negligible impact on resonant period and quality factor in this system, consistent with the analysis above (conduit-reservoir model analytical solutions under simplified conditions) and in (*20*). We thus fix the compressibility of magma in the reservoir to 5×10^{-10} Pa^{-1}.

Fig. S9 shows the effects of various magma system geometries and magma properties on resonant period, quality factor, and conduit bottom magmastatic pressure load (equal to pressure at the top of Halemaʻumaʻu reservoir). For comparison, Fig. S10 shows simulations where magma density and viscosity are directly prescribed following piecewise linear depth functions. In this case lava lake elevation and magma properties in the lava lake do not appreciably effect resonant period or quality factor (Fig. S10) because the much larger cross-sectional area of the lava lake relative to the conduit means that the viscous damping, inertial, and gravitational terms are comparatively minimal in the lava lake. However, in the volcanologically informed background state lava lake elevation and magma properties in the lava lake do affect period and quality factor. These parameters change the magmastatic pressure load on the conduit, thus changing volatile solubility and gas density. This illustrates one important advantage of using the volcanologically informed background state model.

GNSS inversions for reservoir pressure change

Table S1 details our assumed reservoir geometry. We use daily GNSS solutions due to significant noise in higher frequency GNSS, and the instrumental drift in tilt-meter data that can be significant at timescales of months or longer. We correct GNSS displacements for the steady background flank slip motion using the multi-component (dikes and décollement) dislocation source model of (*57*) which consists of slip along low-angle normal faults as well as opening and strike-slip motion along segments of the east rift zone (Fig. S3).

We find that Fourier domain first-order topography corrections (*70*) change inverted pressures by less than 1%, so we do not include them for consistency with the south flank motion corrections which were derived without topography. For each time t we use a linear least-squares inversion to jointly solve for pressure changes in the two/three reservoirs that best fit the observed displacements $U_{j,k}$ for the east, north and vertical ($k = E, N, Z$) components of $j = 1 : m$ available stations,

$$U_{j,k}(t) = G_{j,k}^{HMM} \Delta P^{HMM}(t) + G_{j,k}^{SCR} \Delta P^{SCR}(t) + G_{j,k}^{INT} \Delta P^{INT}(t), \tag{41}$$

where G^{HMM}, G^{SCR}, and G^{INT} and are halfspace quasistatic elastic Green's functions for the Halema'uma'u reservoir, South Caldera reservoir, and 2015 intrusion respectively (*62*), and ΔP^{HMM}, ΔP^{SCR}, and ΔP^{INT} are pressure changes.

VLP event inversions for magma properties

Table S1 lists reference values of all fixed parameters used for these inversions. We linearly interpolate between lava lake surface elevation and surface area measurements in (*4, 32*) to directly prescribe lava lake surface elevation and effective lava lake radius (assuming a circular lava lake surface) at the time of each VLP event. We do not interpolate lava lake bottom elevation since there are only two measurements in 2011 and 2018 (*4*). To obtain the target conduit bottom pressure at the time of each VLP event, we add an assumed baseline pressure to our geodetically inverted Halema'uma'u reservoir pressure changes and linearly interpolate to the time of VLP events (see section below on inversions with different fixed parameters).

We note that exact solutions to the data do not imply zero uncertainty, as there is uncertainty in the data. Uncertainty in VLP event ω and Q depends upon factors such as the signal/noise ratio of each event, and is highly variable (*22*). We use only the more robustly resolved events, for which uncertainty in ω is $\sim$2-4% of the inverted values of ω. Uncertainty in Q is more difficult to robustly quantify, but we estimate it to be $\sim$5-50%. Uncertainty in GNSS displacements is $\sim$0.001 m (*61*); $\sim$0.1% of the total displacements from 2008-2018 ($\sim$1 m) and $\sim$10% of the maximum daily displacements ($\sim$0.01 m). Uncertainty in inverted reservoir pressure changes (as a percentage) will be of a similar order of magnitude to the uncertainty in GNSS data. Uncertainty in lava lake elevation measurements is 1-5 m (*4, 32*). Additional uncertainty is also present in reservoir pressure and lava lake elevation from interpolating these data to the time of each VLP event.

Uncertainty in Q by far dominates the total data uncertainty. Since temperature in our inversions results is primarily a function of Q, uncertainty in temperature will be dominated by uncertainty in Q and may be up to $\sim$100 °C. Uncertainty in Q also ends up being the largest contributor to uncertainty in inverted total volatile contents, since variation in inverted temperature induced by uncertainty in Q effects gas density and induces uncertainty of up to $\sim$0.5 wt% in volatile contents. We thus expect that noise in Q contributes to much of the scatter in all inverted magma properties.

Time-series analysis

To mitigate noise in the time-series of inversion results induced by data error, we calculate moving averages with a 30-day triangular weighted moving window. This window was chosen to smooth much of the apparent scatter while preserving trends over timescales of weeks or longer.

To produce uniformly sampled data for frequency analysis, we first linearly interpolate all data sets at 1 hr increments. We use continuous wavelet transforms with Morlet wavelets (since our time series are non-stationary) for each individual data set, and continuous wavelet magnitude-squared coherence and cross spectra between each pair of data sets (e.g., Fig. S7). We then calculate mean values across the timeline at each frequency in a continuous wavelet transform or continuous wavelet coherence to estimate the overall spectrum or coherence. To obtain the overall cross spectrum we use a weighted mean based on the magnitude-squared coherence at each time and frequency, which ensures that the overall values more strongly reflect the times where signals are more coherent.

To estimate 95% significance thresholds for coherence, we generate 10000 pairs of synthetic Gaussian white noise and compute coherence between each pair following the methods above (*71*). The 95% threshold for each frequency is then taken to be the 95th quantile of coherence at that frequency (i.e., there is only a 5% chance that values above this threshold could be random noise rather than coherent signals).

Inversions with different fixed parameters

Here we only consider variation in the fixed parameters that are most poorly constrained and/or that have the largest effect on inverted magma properties, and we focus on the effects of changing each parameter in isolation. Fig. S5 shows these effects relative to the reference values in Table S1.

We find empirically that South Caldera reservoir centroid depth and aspect ratio (height/width) have nearly identical impacts on inverted Halemaʻumaʻu reservoir pressure changes (hence on inverted magma properties), so we only show the former. Decreasing either parameter causes the inversions to assign more of the long-term deformation to the Halemaʻumaʻu reservoir. We find that the South Caldera reservoir needs to be relatively deep and/or vertically elongated to produce time-series of pressure in the Halemaʻumaʻu reservoir that are consistent with observed lava lake elevation. For example, we show approximate bounds on such magmastatic pressure changes in Fig. S4 that were calculated assuming lower and upper bounds on average magma column densities of 1000 and 2700 kg/m^3. Since previous studies have found either vertically shortened or spherical South Caldera reservoir geometries, we assume a reference spherical geometry. The volume of a spherical reservoir does not significantly effect ground deformation patterns (*63*) and thus does not impact inverted Halemaʻumaʻu reservoir pressure, so we fix the South Caldera reservoir volume to 20 km^3 (*58*). Previous studies find centroid elevations ranging from -2 to -4 km ASL (*7, 10, 58, 59*), so we choose a reference of -3 km ASL. Decreasing this to -4 km ASL has a negligible impact on temperature, increases X^{avg} by $\sim$0.3 wt% by the end of the timeline, and decreases ΔX by $\sim$0.4 wt% by the end of the timeline. Increasing this to -2 km ASL has a negligible impact on temperature, decreases X^{avg} by $\sim$1 wt% by the end of the timeline, and increases ΔX by $\sim$0.6 wt% by the end of the timeline. We also note that this shallower South Caldera reservoir causes a strong trend in Halema‘uma‘u reservoir pressure such that these inversions are not able to exactly fit both pressure and ω after 2016 without invoking magma densities in excess of the pure melt density at the base of the conduit.

Minimal direct constraints exist on possible values for H_2O/CO_2 mass ratio in the shallow magma system since many of the volatiles (particularly CO_2) are exsolved. Estimates of the volatile mass ratio in primitive/parent magma at depth vary but are typically around 1 (*36*). Significant outgassing of CO_2 at depth results in estimated Halema‘uma‘u gas emission H_2O/CO_2 mass ratios that are highly variable but up to 30, and Halema‘uma‘u melt inclusion and glass compositions show a wide range of H_2O/CO_2 mass ratios (*13, 36*). We thus chose an intermediate reference H_2O/CO_2 mass ratio of 3 (or 1 wt% H_2O-to-4.7×10^3 ppm CO_2). Decreasing the mass ratio to 1 uniformly increases temperature by $\sim$10 °C, uniformly increases X^{avg} by $\sim$0.8 wt%, and uniformly increases ΔX by $\sim$0.6 wt%. Increasing the mass ratio to 20 uniformly decreases temperature by $\sim$10 °C, uniformly decreases X^{avg} by $\sim$0.4 wt%, and uniformly decreases ΔX by $\sim$0.4 wt%. We set the baseline Halema‘uma‘u reservoir top pressure relative to the time of the Mar 7, 2011 lava lake draining (Fig. S4). Bounds on this baseline can be obtained by considering magmastatic pressure from feasible conduit average magma densities (say 400-2600 kg/m^3). However, we find that many baseline pressures that are feasible at this particular time would require unfeasibly high or low magma densities in some part of the conduit at other times. We choose a reference baseline Halema‘uma‘u reservoir top pressure of 2.3 MPa that corresponds to an average magma column density of 800 kg/m^3 at the time of the Mar 7, 2011 lava lake draining; this produces feasible densities/volatile mass fractions over all of the timeline after 2010. Decreasing baseline pressure to 2.0 MPa (average magma column density of 700 kg/m^3) uniformly increases temperature by $\sim$10 °C, uniformly increases X^{avg} by $\sim$0.2 wt%, and uniformly decreases ΔX by $\sim$0.2 wt%. Increasing baseline pressure to 2.6 MPa (average magma column density of 900 kg/m^3) uniformly decreases temperature by $\sim$10 °C, uniformly decreases X^{avg} by $\sim$0.2 wt%, and uniformly increases ΔX by $\sim$0.2 wt%.

We choose a reference conduit radius of 15 m, which produces temperatures generally consistent with or less than geochemically inferred Halema‘uma‘u reservoir values (which we assume represent an approximate upper bound on plausible conduit temperatures) (*7, 13, 24*). Decreasing the conduit radius to 5 m uniformly increases temperature by $\sim$50 °C, uniformly decreases X^{avg} by $\sim$0.1 wt%, and has a negligible impact on ΔX. Increasing the conduit radius to 25 m uniformly decreases temperature by $\sim$30 °C, uniformly increases X^{avg} by $\sim$0.1 wt%, and has a negligible impact on ΔX.

We choose a reference conduit length of 290 m, which is consistent with a vertical connection between the Halema‘uma‘u reservoir geometry we adopt from (*11*) and our assumed lava lake base elevation of 700 m ASL. We explore the effect of varying conduit length by varying lava lake base elevation, noting that varying the reservoir top elevation would have a roughly similar effect (Fig. S9). Decreasing the conduit length to 190 m uniformly decreases temperature by $\sim$20 °C, uniformly increases X^{avg} by $\sim$0.2 wt%, and uniformly increases ΔX by $\sim$0.5 wt%. Increasing the conduit length to 390 m uniformly uniformly increases temperature by ∼20 °C, has a negligible impact on X^{avg} (except in the earliest part of the timeline), and uniformly decreases ΔX by ∼1 wt%.

Available continuous gravity data suggest that the top of the lava lake is a foam with porosity of 92-96%, varying on timescales of hours with episodic 'gas-pistoning' events (*4, 37*). We chose a reference lava lake top volatile contents of 1.8 wt%, corresponding to a porosity of ∼93%. Decreasing lava lake top volatile contents to 1 wt% uniformly increases temperature by ∼10 °C, uniformly increases X^{avg} by ∼0.8 wt%, and uniformly increases ΔX by ∼0.4 wt%. Increasing lava lake top volatile contents to 2.6 wt% uniformly decreases temperature by ∼10 °C, uniformly decreases X^{avg} by ∼0.4 wt%, and uniformly decreases ΔX by ∼0.4 wt%.

Additional coherence and phase lag calculations

Fig. S6 and Fig. S7 show additional coherence and phase lag plots.

Inversions for direct values of magma density and viscosity

We show results from inversions for magma density and viscosity in Fig. S8. This provides context for the inversions for volatile contents and temperature we focus on in the main text, and facilitates comparison with inversions for isolated VLP events in (*9*). For these inversions we assume a uniform magma viscosity and a fixed magma density at the top of the lava lake, analogous to the assumptions we made in temperature and volatile content inversions. The three free parameters are then: (1) magma density at the conduit top, (2) magma density at the conduit bottom, and (3) uniform magma viscosity. Density is also shown in Fig. S9 as the average value in the conduit and the difference between the top and bottom of the conduit.

There is over an order of magnitude of variation in inverted viscosity on timescales ranging from days to years. For the majority of the 2009-2018 timespan, magma viscosity exhibits a clear inverse relationship with Q (Fig. S8). This is consistent with the strong impact of viscosity on Q (Fig. S10). Part of the large scatter in viscosity is likely related to noise in the estimates of Q (*22*).

Conduit averaged magma density and conduit magma density difference both roughly track lava lake elevation and inverted reservoir pressure. A positive relation between conduit average magma density and lava lake elevation/reservoir pressure is expected since changing lava lake elevation shifts the magma column up or down. Vertical translation of the magma column could also explain the variations observed in density difference if the density gradient is more gradual at greater depths (i.e., nonlinear), which is expected unless volatile contents increase significantly with depth. This dependence of density upon upward/downward shifting of the magma column highlights another important advantage of using volcanologically informed background states to infer changes in properties of interest such as volatile contents.

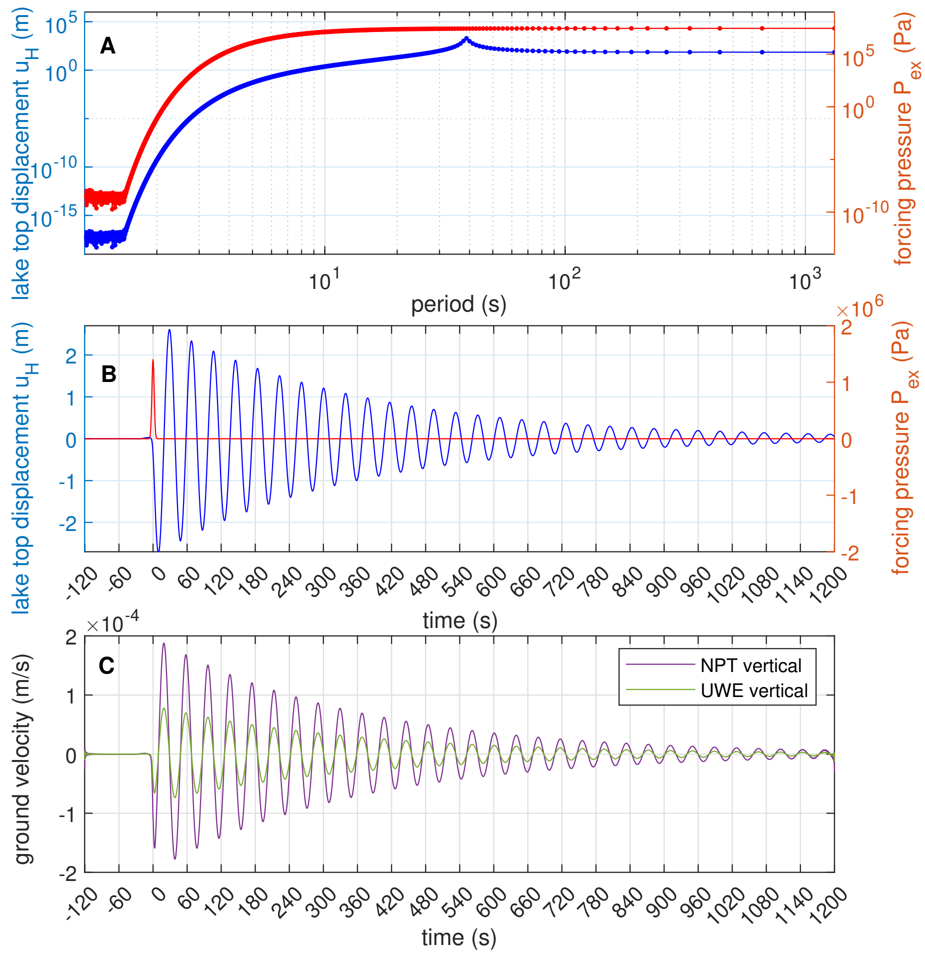

Fig. S1. Example solution to the conduit-reservoir magma resonance model for a Gaussian pressure perturbation with amplitude of 1.4 MPa and variance of 4 s applied to the magma column shown in main text Fig. 1. (**A**) Lava lake top displacement and forcing pressure in the frequency domain. (**B**) Lava lake top displacement and forcing pressure in the time domain. (**C**) Vertical ground velocities at the locations of two nearby seismometers.

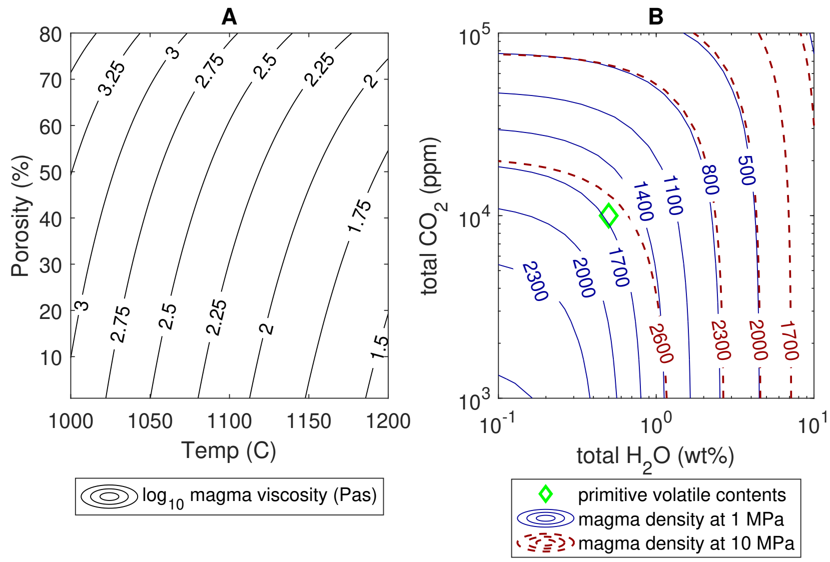

Fig. S2. (**A**) Variation of magma viscosity with temperature and porosity, adopted from (*22*). (**B**) Variation of magma density with H_2O and CO_2 contents at two pressures (1 and 10 MPa correspond to magmastatic depths of 40-100 m and 0.4-1 km respectively) and a temperature of 1100 °C. The density of pure melt is $\sim$2650 kg/m^3. Estimated primitive (or 'parent') magma total volatile contents from (*36*).

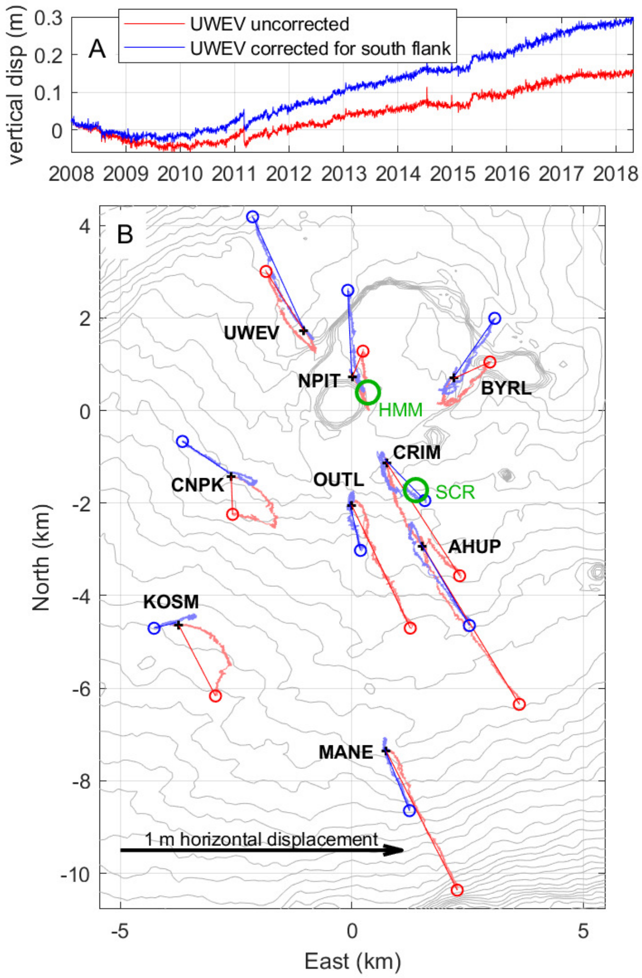

Fig. S3. (**A**) Vertical ground displacement at GNSS station UWEV. (**B**) Map of GNSS stations and horizontal ground displacements from 2008-2018. Red lines are corrected for flank motion and blue are uncorrected. Lighter red and blue lines show the GNSS displacement over time from Jan 1, 2008 (black plus symbols) to May 1, 2018 (red and blue circles). Straight red and blue lines show the net 2008 to 2018 displacement vectors. The inferred centroid locations of the Halema‘uma‘u (HMM) and South Caldera (SCR) reservoirs are shown by green circles. UTM zone 5Q.

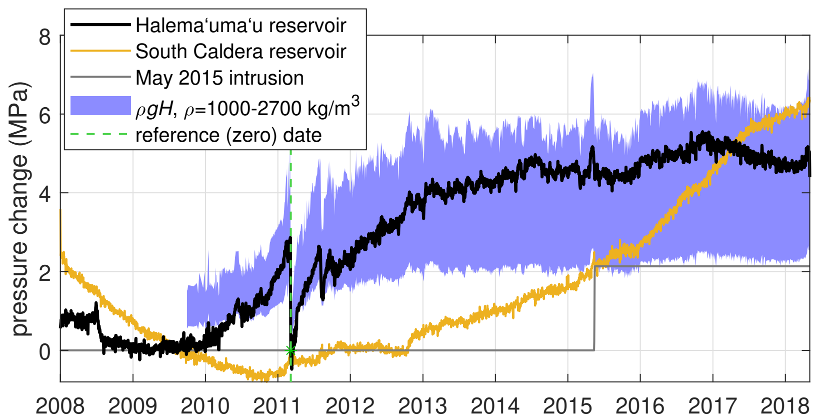

Fig. S4. Joint GNSS inversions for pressure change over 2008-2018 compared to magmastatic pressure changes calculated from lava lake elevation data (*4, 32*) with assumed average magma column densities ρ of 1000 and 2700 kg/m^3 (approximate lower and upper bounds).

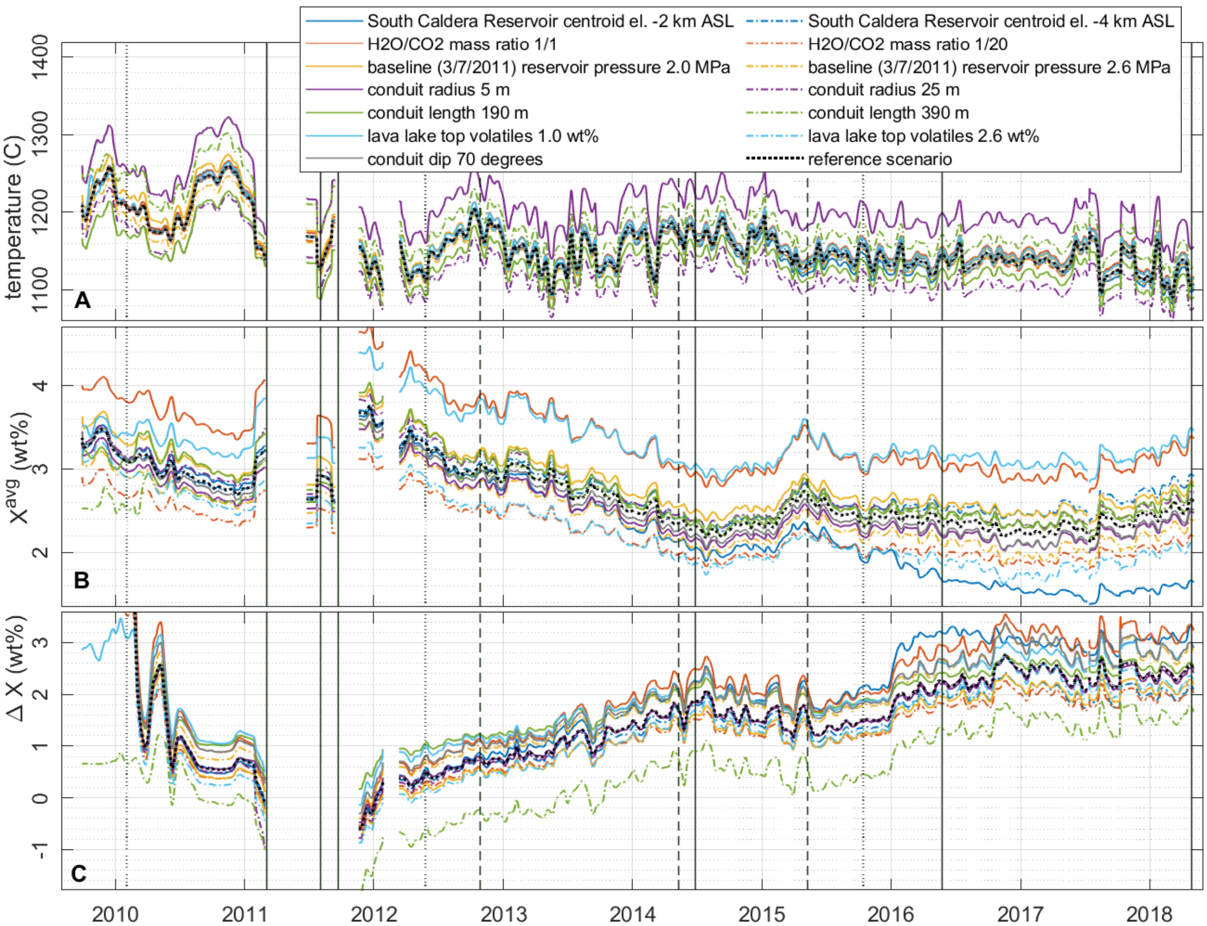

Fig. S5. Inversions with different fixed parameter values. The legend indicates the one fixed parameter value changed to produce each solid colored line; all other fixed parameters are held equal to the reference values from Table S1. Vertical black lines are East Rift Zone eruptions (solid), summit intrusions (dashed), and slow-slip events (dotted) (*4*). Values from 2009-early 2010 are unreliable due to exact solutions not being obtainable with the fixed parameter combinations shown.

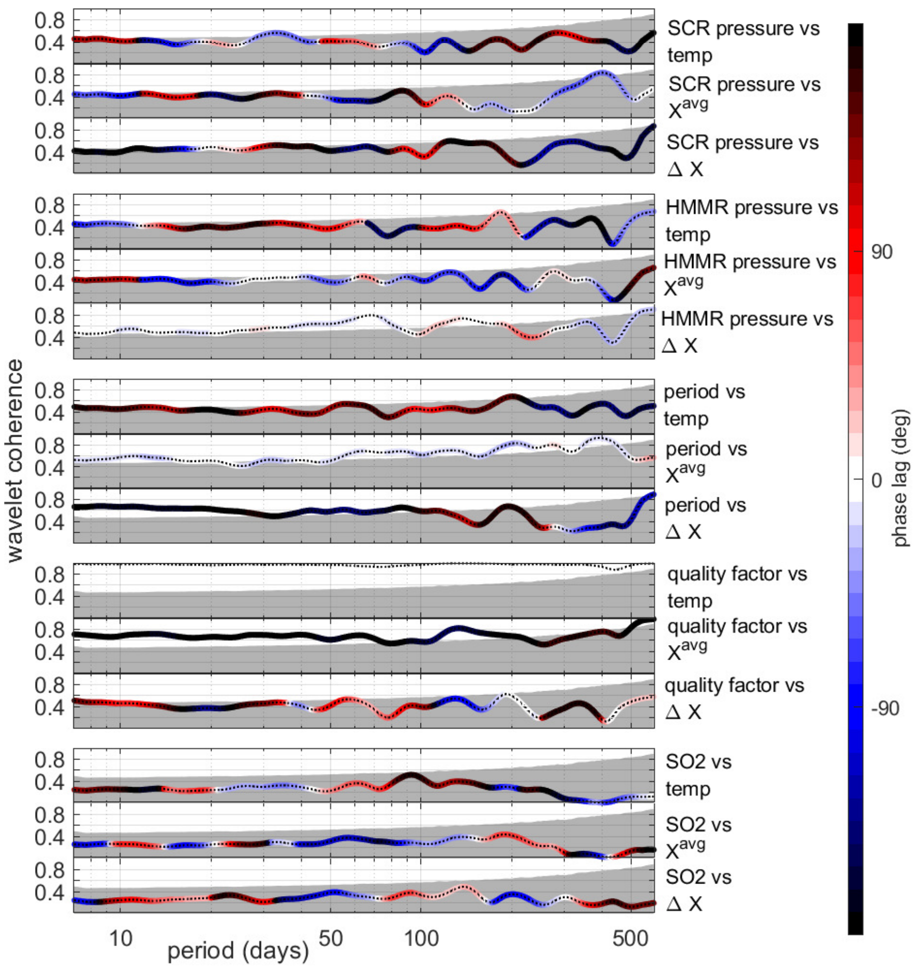

376 **Fig. S6.** Magnitude squared coherence colored by phase lag. The gray area is beneath the 95% significance threshold. Positive phase lags indicate that the second variable trails the first. Data before Dec 2011 were excluded from this analysis.

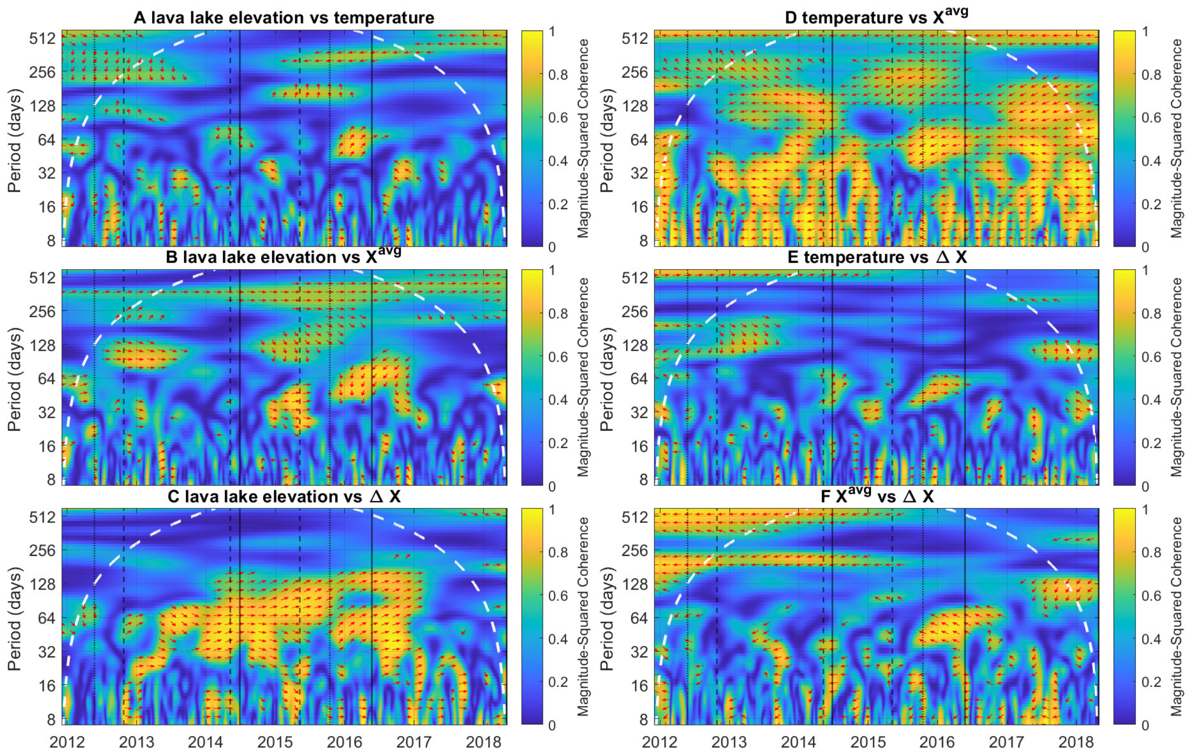

Fig. S7. Spectral coherence and phase lags between lava lake elevation (*4, 32*) and volatile-based magma properties. Red arrows indicate the direction of phase lag where coherence is greater than 0.5; right indicates in-phase (positive correlation), left indicates 180 degrees out of phase (negative correlation), and up or down indicates 90 degrees out of phase. The white region in 2011 was excluded due to limited data. Dashed white lines indicate the region of edge influence. Vertical black lines are East Rift Zone eruptions (solid), summit intrusions (dashed), and slow-slip events (dotted) (*4*).

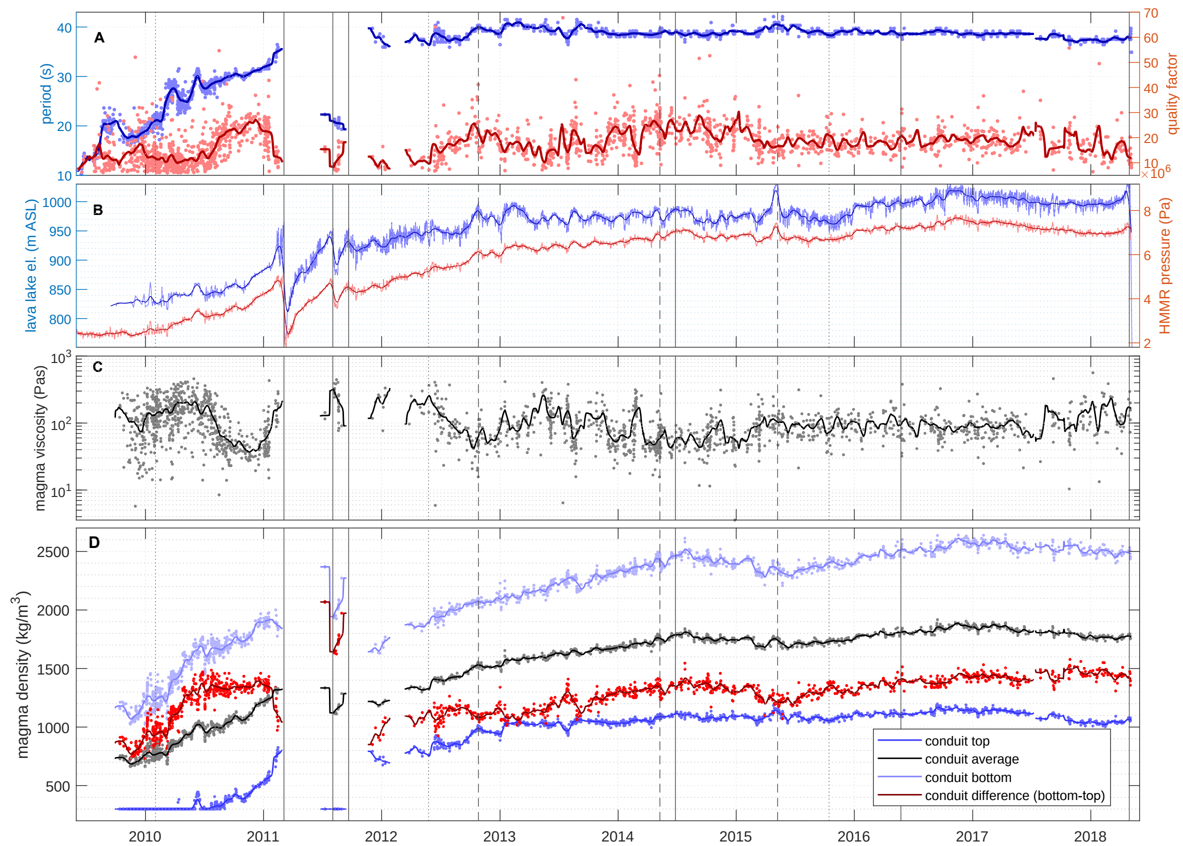

Fig. S8. Inverted relative changes in magma properties for our reference fixed parameter values (Table S1) without parameterization in terms of temperature and volatile contents. Dots represent individual VLP events, bold lines are 30-day moving averages, while vertical black lines are East Rift Zone eruptions (solid), summit intrusions (dashed), and slow-slip events (dotted) (*4*). (**A**) VLP period and quality factor (*22*). (**B**) Lava lake elevation (*4,32*) and geodetically inverted reservoir pressure changes, relative to the time of the Mar 7, 2011, lava lake draining. (**C**, **D**) Inverted magma properties.

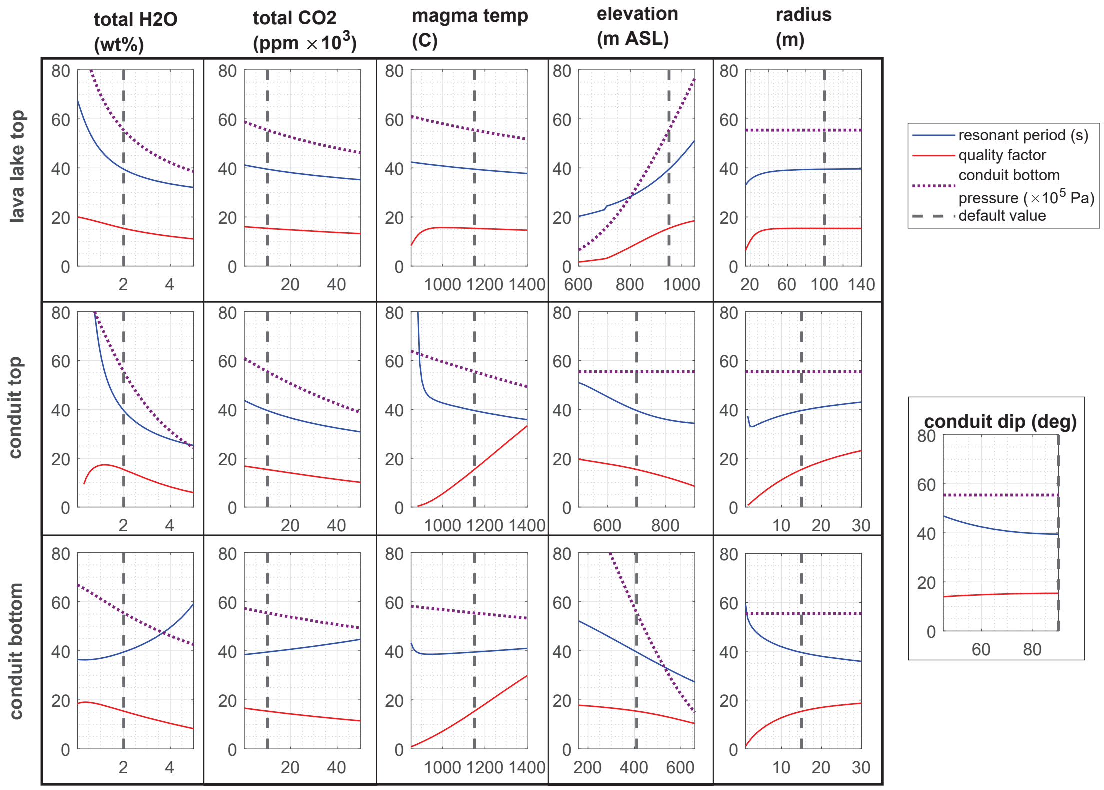

Fig. S9. Predicted variation in resonance period, quality factor, and pressure at the bottom of the conduit (or top of the reservoir) due to varying model parameters in isolation. Dashed black lines indicate the default value of each parameter used to make the other plots. We do not show parameters related to reservoir storativity (reservoir shape, host rock shear modulus, and magma compressibility in the reservoir) since they have a negligible impact on these simulations. We note that conduit bottom elevation is the same as reservoir top elevation and that we have assumed a cylindrical lava lake.

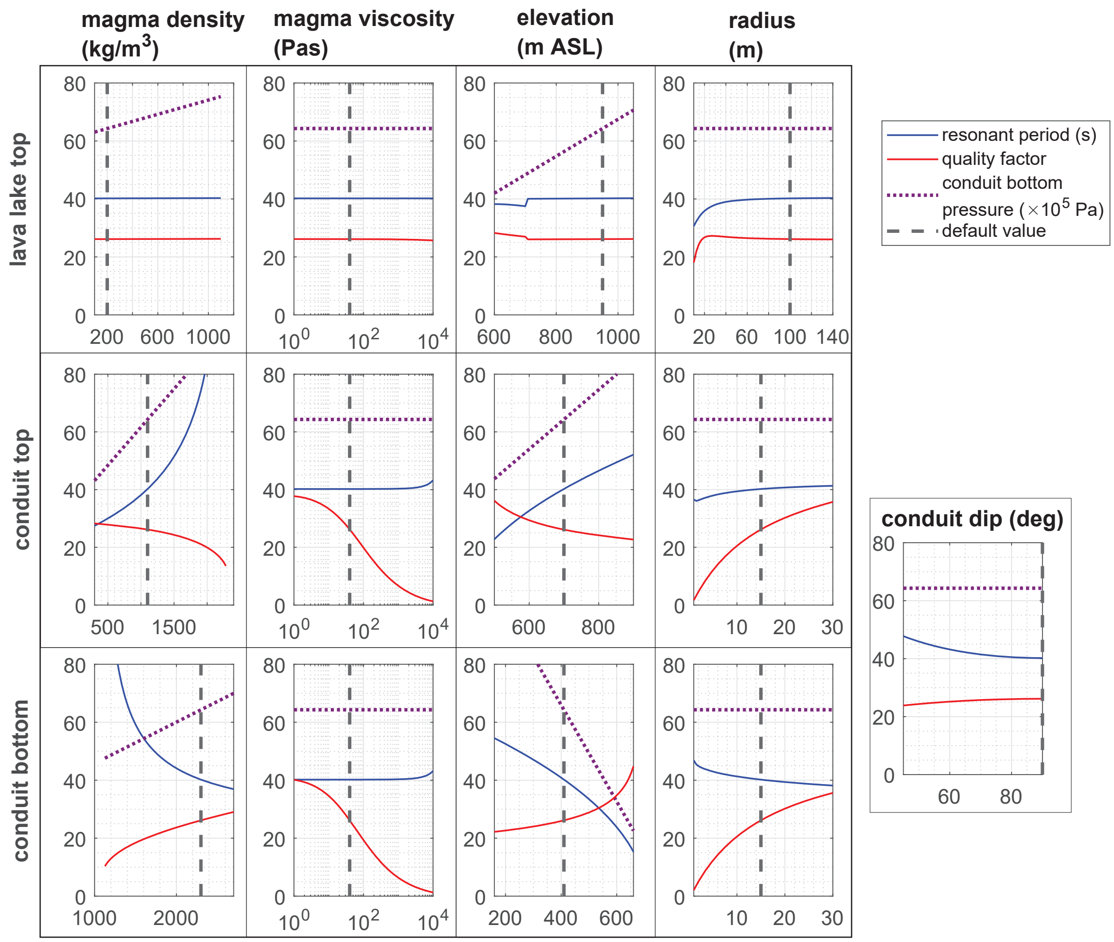

Fig. S10. Predicted variation in resonance period, quality factor, and pressure at the bottom of the conduit (or top of the reservoir) due to varying model parameters in isolation without parameterization in terms of temperature and volatile contents. Dashed black lines indicate the default value of each parameter used to make the other plots. We do not show parameters related to reservoir storativity (reservoir shape, host rock shear modulus, and magma compressibility in the reservoir) since they have a negligible impact on these simulations. We note that conduit bottom elevation is the same as reservoir top elevation and that we have assumed a cylindrical lava lake.

	parameter	default value	units
	Conduit + lava lake geometry		
	lava lake top elevation	prescribed from (*4, 32*)	m ASL
	lava lake bottom elevation	700	m ASL
	conduit bottom elevation	410	m ASL
H	total (conduit + lava lake) length	calculated	m
R_H	lava lake radius	prescribed from (*4, 32*)	m
	conduit top radius	15	m
R_0	conduit bottom radius	15	m
θ	conduit dip (from horizontal)	90	degrees
	Magma reservoirs		
G	rock shear modulus	3.08	GPa
	Halema‘uma‘u reservoir geometry	fixed from (*11*)	
	2015 intrusion geometry	fixed from (*27*)	
	South Caldera reservoir centroid elevation	-3000	m ASL
	South Caldera reservoir centroid latitude	19.3900	degrees
	South Caldera reservoir centroid longitude	-155.2710	degrees
	South Caldera reservoir volume	20	km^3
	South Caldera reservoir aspect ratio	1	
	Magma properties		
β_m	Halema‘uma‘u reservoir magma compressibility	5×10^{-10}	Pa^{-1}
	H_2O/CO_2 mass ratio	3	
	lava lake top volatiles	1.8	wt%
	melt composition	fixed from (*13*)	
ρ_l	melt density	calculated from (*29*)	
μ_l	melt viscosity	calculated from (*31*)	
	H_2O-CO_2 solubility	calculated from (*25*)	
	Other		
P_{atm}	atmospheric pressure	10^5	Pa
p_0	baseline (Mar 7, 2011) conduit bottom pressure	2.3	MPa
g	gravitational acceleration	9.81	m/s^2
R_g	ideal gas constant	8.314	Jkg^{-1}mol^{-1}

Table S1. Reference model parameter values